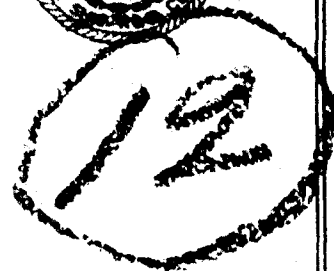


AD A013598

# NAVAL SHIP RESEARCH AND DEVELOPMENT CENTER

Bethesda, Md. 20084



## AERODYNAMIC CHARACTERISTICS OF A $10^\circ$ SHARP CONE AT HYPERSONIC SPEEDS AND HIGH ANGLES OF ATTACK

by

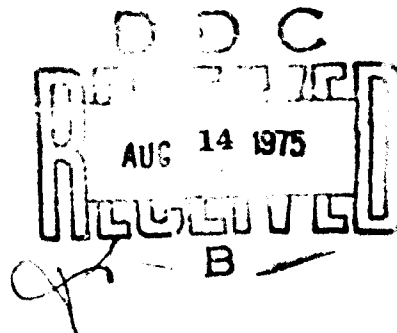
George S. Pick  
Samuel E. Dawson  
Robert L. Walker

APPROVED FOR PUBLIC RELEASE: DISTRIBUTION UNLIMITED

REPRINT FROM THE 9TH NAVY SYMPOSIUM ON AEROBALLISTICS,  
APPLIED PHYSICS LABORATORY, THE JOHNS HOPKINS UNIVERSITY,  
9-11 May 1972

AVIATION AND SURFACE EFFECTS DEPARTMENT  
RESEARCH AND DEVELOPMENT REPORT

June 1975

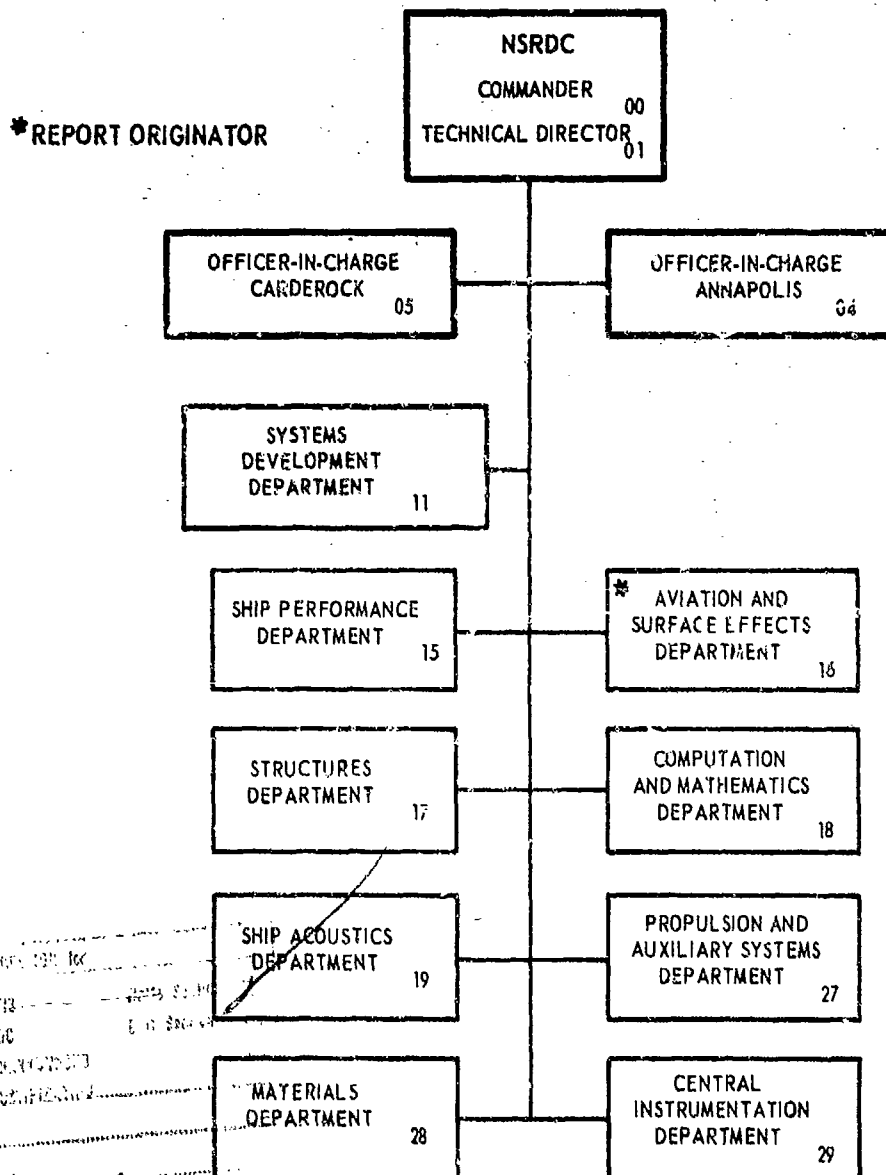


Report 4692

The Naval Ship Research and Development Center is a U. S. Navy center for laboratory effort directed at achieving improved sea and air vehicles. It was formed in March 1967 by merging the David Taylor Model Basin at Carderock, Maryland with the Marine Engineering Laboratory at Annapolis, Maryland.

Naval Ship Research and Development Center  
Bethesda, Md. 20084

### MAJOR NSRDC ORGANIZATIONAL COMPONENTS



UNCLASSIFIED

SECURITY CLASSIFICATION OF THIS PAGE (When Data Entered)

19 REPORT DOCUMENTATION PAGE		READ INSTRUCTIONS BEFORE COMPLETING FORM	
1. REPORT NUMBER NSRDC 4692	2. GOVT ACCESSION NO. deg	3. RECIPIENT'S CATALOG NUMBER 9	
4. TITLE (and Subtitle) AERODYNAMIC CHARACTERISTICS OF A 10° SHARP CONE AT HYPERSONIC SPEEDS AND HIGH ANGLES OF ATTACK		5. TYPE OF REPORT & PERIOD COVERED Final Report	
7. AUTHOR(s) George S. Pick, Samuel E. Dawson and Robert L. Walker		6. PERFORMING ORG. REPORT NUMBER 14 Aero 1211	
9. PERFORMING ORGANIZATION NAME AND ADDRESS Naval Ship Research and Development Center Bethesda, Maryland 20084		10. PROGRAM ELEMENT, PROJECT, TASK AREA & WORK UNIT NUMBERS 61102N R009-0201	
11. CONTROLLING OFFICE NAME AND ADDRESS Naval Air Systems Command (AIR-320C) Washington, D.C. 20361		12. REPORT DATE 12 Jun 75	
14. MONITORING AGENCY NAME & ADDRESS (if different from Controlling Office)		13. NUMBER OF PAGES 25	
16. DISTRIBUTION STATEMENT (of this Report) APPROVED FOR PUBLIC RELEASE: DISTRIBUTION UNLIMITED		15. SECURITY CLASS. (of this report) UNCLASSIFIED	
17. DISTRIBUTION STATEMENT (of the abstract entered in Block 20, if different from Report)			
18. SUPPLEMENTARY NOTES Presented at the 9th Navy Symposium on Aeroballistics, Applied Physics Laboratory, The Johns Hopkins University, 9-11 May 1972.			
19. KEY WORDS (Continue on reverse side if necessary and identify by block number) Hypersonic Flow High Angle of Attack Aerodynamics Free Flight Data Lift, Drag Characteristics → 1,200,000 ft			
20. ABSTRACT (Continue on reverse side if necessary and identify by block number) A free-flying instrumented model was tested in a hypersonic facility at $M = 5.30, 6.34$ and $9.94$ and $Re = 6 \times 10^5$ to $1.2 \times 10^6$ /ft. Aerodynamic lift, total drag and base drag coefficients were obtained together with detailed base pressure distribution measurements at angles of attack from $0$ to $60^\circ$ . The measured lift and drag coefficients showed good agree- ment with the modified Newtonian theory. The centerline $(P_B/P_\infty)$ distribution was nearly independent of the angle of attack from $-10$ to $-30^\circ$ but increased rapidly → -30 DEG (Continued on reverse)			

DD FORM 1 JAN 73 1473

EDITION OF 1 NOV 68 IS OBSOLETE  
S/N 0102-014-6601

UNCLASSIFIED

SECURITY CLASSIFICATION OF THIS PAGE (When Data Entered)

300900

BASE PRESSURE / FREE-STREAM STATIC PRESSURE  
→ PSIA

UNCLASSIFIED

SECURITY CLASSIFICATION OF THIS PAGE(When Data Entered)

Block 20 (Continued)

*→ alpha = -30 deg*

for all test conditions beyond  $\alpha = -30^\circ$ . For similar conditions at angle of attack and Reynolds number, an increase in Mach number resulted in an increase of the base pressure ratio. The measurements indicated a highly complex base flow region, and tentative explanation of the observed results was offered.

UNCLASSIFIED

SECURITY CLASSIFICATION OF THIS PAGE(When Data Entered)

## TABLE OF CONTENTS

	Page
ABSTRACT . . . . .	1
NOMENCLATURE . . . . .	1
INTRODUCTION . . . . .	2
BACKGROUND . . . . .	2
TEST APPARATUS, EXPERIMENTAL TECHNIQUES, TEST CONDITIONS . . . . .	4
WIND-TUNNEL FACILITY . . . . .	4
MODEL DESCRIPTION . . . . .	4
INSTRUMENTATION AND DATA ACQUISITION SYSTEM . . . . .	5
Pressure Sensors . . . . .	5
Antenna Geometry . . . . .	5
Drop Mechanism . . . . .	5
Signal Processing and Data Acquisition . . . . .	6
PRELIMINARY SYSTEM STUDIES . . . . .	6
Pressure-Time Response . . . . .	6
Transducer Interactions and Calibration . . . . .	6
TEST CONDITIONS . . . . .	7
TEST PROGRAM . . . . .	7
DATA REDUCTION . . . . .	7
REDUCTION OF HIGH-SPEED MOTION PICTURE DATA . . . . .	7
BASE PRESSURE AND FORCE REDUCTION PROGRAM . . . . .	9
DISCUSSION OF RESULTS . . . . .	10
BASE PRESSURE DISTRIBUTION . . . . .	10
AERODYNAMIC COEFFICIENTS AT THE MODEL BASE . . . . .	12
TOTAL DRAG AND LIFT COEFFICIENTS . . . . .	12
MODEL TRAJECTORY RESULTS . . . . .	13
CONCLUSIONS . . . . .	13
REFERENCES . . . . .	13

## LIST OF FIGURES

	Page
1 - Exploded View of Instrumented $10^\circ$ Half-Angle Cone Base Pressure Model . . . . .	15
2 - Schematics of Model Interior . . . . .	15
3 - Instrumented Cone Model and Antenna Installed in Hypersonic Tunnel . . . . .	15
4 - Terminal Release Velocity and Trigger Switch Location as Functions of Model Drop Height . . . . .	15
5 - Block Diagram of $10^\circ$ Cone Model and its Instrumentation in the Hypersonic Wind Tunnel . . . . .	15
6 - Sample Oscillograph Record . . . . .	15
7 - Time Response Characteristics of the Transducer System . . . . .	16
8 - Centerline Base Pressure Ratio as Function of Angle of Attack and Mach Number at $Re = 1 \times 10^6/ft$ . . . . .	16
9 - Centerline Base Pressure Ratio as Function of Angle of Attack and Mach Number at $Re = 6 \times 10^5/ft$ . . . . .	16
10 - Centerline Base Pressure Ratio as Function of Angle of Attack at $M = 6.34$ and $Re = 3 \times 10^5/ft$ . . . . .	16
11 - Base Pressure Distribution in the Vertical Meridian Plane at $M = 6.34$ . . . . .	17
12 - Base Pressure Distribution in the Vertical Meridian Plane at $M = 5.30$ . . . . .	17
13 - Base Pressure Distribution in the Vertical Meridian Plane at $M = 9.94$ . . . . .	17
14 - Base Pressure Distribution at $M = 6.34$ and $Re = 6.2 \times 10^5/ft$ . . . . .	17
15 - Base Pressure Distribution at $M = 5.30$ and $Re = 5.9 \times 10^5/ft$ . . . . .	17
16 - Base Pressure Distribution at $M = 9.94$ and $Re = 6.4 \times 10^5/ft$ . . . . .	17
17 - Base Pressure Coefficients as Functions of Angle of Attack and Mach Number at $Re \approx 6 \times 10^5/ft$ . . . . .	17
18 - Base Pressure Coefficients as Functions of Angle of Attack and Mach Number at $Re \approx 1 \times 10^6/ft$ . . . . .	18
19 - Base Drag Coefficients as Functions of Angle of Attack and Mach Number at $Re \approx 6 \times 10^5/ft$ . . . . .	18
20 - Base Drag Coefficients as Functions of Angle of Attack and Mach Number at $Re \approx 1 \times 10^6/ft$ . . . . .	19

	Page
21 - Base Lift Coefficients as Functions of Angle of Attack and Mach Number at $Re \approx 6 \times 10^5/ft$ . . . . .	19
22 - Base Lift Coefficients as Functions of Angle of Attack and Mach Number at $Re \approx 1 \times 10^6/ft$ . . . . .	19
23 - Total Drag Coefficient as Function of Angle of Attack and Reynolds Number at $M = 5.30$ . . . . .	19
24 - Total Drag Coefficient as Function of Angle of Attack and Reynolds Number at $M = 6.34$ . . . . .	19
25 - Total Drag Coefficient as Function of Angle of Attack and Reynolds Number at $M = 9.94$ . . . . .	20
26 - Total Lift Coefficient as Function of Angle of Attack and Reynolds Number at $M = 5.30$ . . . . .	20
27 - Total Lift Coefficient as Function of Angle of Attack and Reynolds Number at $M = 6.34$ . . . . .	20
28 - Total Lift Coefficient as Function of Angle of Attack and Reynolds Number at $M = 9.94$ . . . . .	20
29 - Measured and Computed Model Trajectories at $M = 5.30$ and $Re = 5.9 \times 10^5/ft$ . . . . .	21
30 - Measured and Computed Model Trajectories at $M = 6.34$ and $Re = 6.2 \times 10^5/ft$ . . . . .	21
31 - Measured and Computed Model Trajectories at $M = 9.94$ and $Re = 11.4 \times 10^5/ft$ . . . . .	21

---

Table 1 - Test Program . . . . .	7
----------------------------------	---

AERODYNAMIC CHARACTERISTICS OF A  $10^\circ$  SHARP CONE AT  
HYPERSONIC SPEEDS AND HIGH ANGLES OF ATTACK  
(U)

(Paper UNCLASSIFIED)

by

George S. Pick, Samuel E. Dawson, and Robert L. Walker  
Aviation and Surface Effects Department  
Naval Ship Research and Development Center  
Bethesda, Maryland 20034

**ABSTRACT.** A free-flying instrumented model was tested in a hypersonic facility at  $M = 5.30, 6.34$  and  $9.94$  and  $Re = 3 \times 10^5$  to  $1.2 \times 10^6$ /ft. Aerodynamic lift, total drag and base drag coefficients were obtained together with detailed base pressure distribution measurements at angles of attack from  $0$  to  $60^\circ$ . The measured lift and drag coefficients showed good agreement with the modified Newtonian theory. The centerline  $p_B/p_\infty$  distribution was nearly independent of the angle of attack from  $-10$  to  $-30^\circ$  but increased rapidly for all test conditions beyond  $\alpha = -30^\circ$ . For similar conditions at angle of attack and Reynolds number, an increase in Mach number resulted in an increase of the base pressure ratio. The measurements indicated a highly complex base flow region, and tentative explanation of the observed results was offered.

NOMENCLATURE

$a_x$  Horizontal acceleration component of model center of gravity, ft/sec<sup>2</sup>  
 $a_y$  Vertical acceleration component of model center of gravity, ft/sec<sup>2</sup>  
 $B$  Equation (18)  
 $C_A$  Axial force coefficient  
 $C_D$  Total drag coefficient  
 $C_{D_B}$  Base drag coefficient  
 $C_{D_0}$  Drag coefficient at  $\alpha = 0^\circ$   
 $C_L$  Total lift coefficient  
 $C_{L_B}$  Lift coefficient due to model base force

$C_N$  Normal force coefficient  
 $C_{P_B}$  Base pressure coefficient  
 $D$  Base diameter, in.  
 $F_B$  Total base force, lbs  
 $g$  Gravitational acceleration, ft/sec<sup>2</sup>  
 $K$  Model geometry and mass function  
 $L$  Model length, in.  
 $M$  Free-stream Mach number  
 $M_\ell$  Mach number based on local properties  
 $p_B$  Base pressure, psia  
 $p'_B$  Base pressure measured with sting mounted model, psia  
 $\bar{p}_B$  Average base pressure, psia  
 $p_\ell$  Local pressure, psia  
 $p_t$  Total pressure, psia  
 $p_\infty$  Free-stream static pressure, psia  
 $q_\infty$  Free-stream dynamic pressure, psia  
 $r$  Radial distance from the centerline  
 $R$  Base radius  
 $Re$  Unit Reynolds number/ft  
 $Re_D$  Reynolds number based on the base diameter  
 $Re_\ell$  Reynolds number based on local properties  
 $Re_L$  Reynolds number based on length  
 $Re_{t\alpha}$  Transition Reynolds number at angle



## 9th Navy Symposium on Aeroballistics

	of attack
$Re_{to}$	Transition Reynolds number at zero angle of attack
$S_B$	Base area, in <sup>2</sup>
$S_x$	Horizontal component of model center of gravity displacement measured from the model release position, in.
$S_y$	Vertical component of model center of gravity displacement measured from the model release position, in.
$t$	Time, sec or msec
$V_t$	Terminal velocity of model at the end of captured flight, ft/sec or in/sec
$W$	Model weight, lbs
$X_{cg}$	Distance to the center of gravity from the model nose
$X_{cp}$	Distance to the center of pressure from the model nose
$\alpha$	Angle of attack, °
$\beta_u$	Equation (11)
$\theta_c$	Cone half angle, °
$\varphi$	Roll angle, °

### INTRODUCTION

The flow field around a slender body of revolution at high angles of attack in the hypersonic speed regime is highly complex because of interaction, separation, three-dimensional mixing in the various separated regions, vortex generation, etc. The physics, on which any mathematical model must be based, is not well understood here because adequate data are lacking for the separated flow regions surrounding a three-dimensional body. Current theories that attempt to calculate the properties of a near wake flow field postulate the existence of a uniform base pressure distribution at zero angle of attack. By using this basic assumption, investigators then proceed to obtain numerical solutions in the near wake. Little or no data are available on base pressure distribution for high angles of attack and therefore one cannot even define a physically reasonable model to attempt a numerical computation.

The basic objective of the current work was to obtain reliable, interference-free aerodynamics data on a 10° half-angle sharp cone at high angles of attack and at hypersonic speeds with varying Reynolds numbers. To this end, a free-flying instrumented model was developed and tested in a free jet hypersonic facility. It was designed to be in-

jected into the flow field at predetermined angles of attack and roll and to be released with adequate vertical velocity to fly through the test section.

### BACKGROUND

Free-flight techniques to investigate the aerodynamic characteristics of models in hypersonic wind-tunnel facilities have been in use for the past 7-8 years. However, practically all of the experimental information reported in the literature deals with axisymmetric geometries at zero angle of attack.

Griffith and Siler<sup>1</sup> compared drag, lift, moment and heat-transfer data from sting-mounted slender cone models ( $\theta_c = 9$  and  $10^\circ$ ) with free-flight model information at  $\alpha = 0^\circ$  and  $M = 9.8$  to  $20.6$ . Their results showed good agreement between the conical shock theory and measured free-flight viscous drag data at  $M = 10$  and  $\alpha = 0^\circ$ . The total drag was shown to increase with angle of attack at  $M = 10$  and decrease with increasing free-stream unit Reynolds number in the range of  $Re = 2.2 \times 10^5$  to  $5.2 \times 10^5$ /ft.

Welsh et al<sup>2</sup> used a hypervelocity range to obtain free-flight static, dynamic stability, and drag data for  $\theta_c = 10^\circ$  slightly blunted cones at Mach numbers from 6 to 16 and  $Re \approx 7 \times 10^4$  to  $5 \times 10^5$ /ft. Zero lift drag measurements at  $\alpha \approx 0^\circ$  and  $Re \approx 2 \times 10^5$ /ft indicated that  $C_{D0}$  was insensitive to small changes in nose bluntness and decreased with increasing Mach number and Reynolds number.

Ward et al<sup>3</sup> utilized 10° half angle cone models in free flight from  $M = 1.5$  to  $M = 10$  and  $\alpha < 6^\circ$  to measure support-free model drag, damping and pitching moment rate, and centerline base pressure. The total drag at  $\alpha = 0^\circ$  was slightly decreasing with increasing unit Reynolds number in the measured range of  $Re = 2 \times 10^5$  to  $5 \times 10^5$ /ft at  $M = 10$  and decreasing with Mach number from  $M = 4$  to  $10$ . The results indicated drag rise with angle of attack ( $0 < \alpha < 6^\circ$ ) and good agreement between the measured viscous drag and conical shock theory at  $M = 10$ .

Available base flow theories in supersonic flow were summarized by Carpenter and Tabakoff<sup>4</sup> in their comprehensive review of some 175 papers and articles. Base flow theories may be divided into four main groups: semiempirical theories, theories based on the Chapman-Korst model, integral methods, and multimethod base flow theories which attempt to take the dynamics of the recirculating flow

into account.

Practically all of the experimental information reported in the literature deals with axisymmetric geometries at zero angle of attack. The Todisco and Pallone<sup>5</sup> comprehensive summary of experimental work includes near-wake data for a variety of vehicle configurations, free-stream Mach numbers, Reynolds numbers, wall temperature ratios, etc.

A few investigators have obtained some data in the base region of slender cones at angles of attack up to  $10^\circ$ . Schlesinger and Martellucci<sup>6</sup> tested a  $10^\circ$  half-angle cone at  $M_\infty = 6.0$  and at a  $10^\circ$  angle of attack. The free-stream Reynolds number was sufficiently large so that fully turbulent flow was achieved both on the cone surface and in the near wake. Significant changes in the flow field were observed when a configuration was studied at angles of attack other than  $0^\circ$ .

Schmidt and Cresci<sup>7</sup> examined the flow characteristics in the near wake of a  $10^\circ$  half-angle cone at  $M = 7.7$  and at  $10^\circ$  angle of attack for laminar flow. They obtained radial variations of pitot and static pressures at selected axial location in the near wake. Their measurements indicated that the angle of attack produced a region on the leeward side of the cone surface wherein the boundary layer which was originally laminar on the windward side became transitional or turbulent at lower Reynolds numbers than expected from the axisymmetric flow case. This affected the mixing processes and therefore the behavior of the local flow conditions in the wake. In addition, it appeared that vertical inviscid flow above the cone surface caused a large-scale mixing for the angle of attack configuration. Pitot pressure profiles showed that the symmetry axis in the viscous core was displaced toward the leeward side of the cone by about one-tenth of the base diameter. The stagnation pressure ratio increased by a factor of five above the laminar axisymmetric flow conditions.

Martellucci and Schlesinger<sup>8</sup> utilized a  $10^\circ$  half-angle cone at  $0^\circ$  angle of attack and  $M_\infty = 12.3$  to obtain laminar near-wake and base pressure data. They employed a special support system to minimize support interference and measured centerline base pressure, dividing velocity line, and static and total pressure distributions together with static and total temperature distributions in the near wake. The results showed that  $p_B/p_\infty = 0.75 \pm 0.05$ .

Martellucci and Ranlet<sup>9</sup> examined the near

wake of a  $10^\circ$  half-angle cone with various bluntness ratios at  $M = 8, 10$ , and  $12.3$  and  $\alpha = 0^\circ$  with a special compression strut system to minimize support interference. Their measurements showed both laminar and transitional flow conditions. The surveyed regions included the cone surface and base areas, the cone shoulder boundary layer and shock layers, the recirculation region, the shear and mixing layers, and the inviscid supersonic weak-wake region. Axial and radial pressures and temperature profiles were taken with various probes. The base pressure results showed that a slight bluntness had no effect but that a greater bluntness ( $R_n/R_b = 0.15$ ) increased the base pressure level above values for the sharp leading edge. The study showed that  $p_B/p_\infty$  decreased with increasing Reynolds numbers and increased with Mach numbers for a given Reynolds number. The variation in radial pressure for the base was maximum at the centerline and decreased toward the edges. As the Reynolds number increased, the nonuniformity decreased; at turbulent conditions, the base pressure distribution was uniform.

Ward and Choate<sup>10</sup> used a free-flight technique to measure base pressure and base heat transfer on a  $10^\circ$  half-angle cone at  $M = 10$  and  $0^\circ$  angle of attack while the shoulder boundary layer and base region conditions were laminar. The absolute values of the base pressure at  $Re_\ell = 0.5 \times 10^6$  were in the range of  $0.004 \text{ psia} \pm 0.001$ . The model base pressure ratio results showed  $p_B/p_\infty \approx 0.58$  at  $Re_\ell = 0.5 \times 10^6$  with a nearly linearly decline to  $\approx 0.35$  at  $Re_\ell = 2 \times 10^6$ .

Cassanto et al<sup>11</sup> correlated  $0^\circ$  angle of attack free-flight centerline base pressure data for both sharp and blunt  $10^\circ$  half-angle cones at the speed range of  $M = 4$  to  $M = 19$ . Both laminar and turbulent flow conditions were tested and analyzed. The sharp cone data showed strong Reynolds number dependence whereas no such dependence was exhibited for the blunt cone. The level of base pressure for the blunt configuration was higher than for the sharp cone for comparable free-stream conditions of both the laminar and turbulent flows. Laminar flow centerline base pressure correlation exhibited a maximum value where  $p_B/p_\ell$  was a single-valued function of  $M_\ell^2 \cdot Re_\ell$ . This function appeared to relate much of the data in the test program. Base pressure correlation for turbulent flow conditions showed no such maximum but  $p_B/p_\ell$  decreased with increasing  $M_\ell$ .

Much of the published experimental information concerning base flow has been clouded by the uncertainty introduced by

## 9th Navy Symposium on Aeroballistics

model support interference. The sting model support system, in common usage in wind-tunnel measurements, is bound to distort the flow field to some extent; consequently, the reliability of the resulting data might be questionable.

Considerable experimental work on the problem of support interference in supersonic speeds has been done at  $0^\circ$  angle of attack. It has confirmed that the base pressure is strongly influenced by the support interference and can serve as the first indication of flow distortion caused by the presence of model support.<sup>12-21</sup>

On the basis of some data,<sup>15-18</sup> it appears that for laminar flow in the range of  $M = 1.5$  to  $5.0$ , there are critical ratios for both length and diameter. However, whereas the sting length/model diameter ratio increased from  $3.0$  to  $6.0$  between  $M = 1.5$  and  $5.0$ , the critical sting diameter/model diameter ratio had a maximum value of  $0.5$  at  $M \approx 4.0$ , and decreased with both increasing and decreasing Mach number. Whitfield<sup>20</sup> states that the sting diameter effects may be important when attempting to correlate data with free-flight results.

Peckham<sup>22</sup> conducted a qualitative exploratory study at  $M = 6.8$  where transition occurred upstream of the model base so that a turbulent wake was formed. He found that at  $\alpha = 20^\circ$ , the flow pattern on a delta wing model was not affected by sting diameter in the range of  $0.4 < d/D < 0.6$ .

In their experimental study with a sharp  $5.6^\circ$  half-angle cone at  $M = 14$ , Stetson and Friberg<sup>22</sup> found that there was no subsonic communication between the base and leeward regions and, consequently, little interaction up to an angle of attack of approximately three times the cone half-angle. However, beyond this incidence angle, the leeside minimum pressure region was reduced to base pressure level and thus there was subsonic communication between these two flow fields. This means that at large angles of attack, any type of mechanical support system will disturb the flow field upstream as well as downstream.

Pick<sup>23</sup> recently investigated the sting effects on measured base pressures at  $M = 6.3$  and  $9.9$  for a unit Reynolds number of  $1 \times 10^8/\text{ft}$ . Sting-mounted and instrumented free-flight half-angle sharp cone models were used between  $\alpha = 0$  and  $\alpha = 40^\circ$ . Measurements showed that the sting-interference effects were not very severe at  $M = 6.3$  where  $\alpha < 15^\circ$  ( $1 < p_B/p_B' < 1.2$ ), but that the flow became progressively more distorted as the angle of

attack increased; at  $\alpha = 40^\circ$ ,  $p_B/p_B' \approx 1.75$ . For the free-flight model at Mach number  $9.9$ , the magnitude of the measured base pressure ratios at corresponding flow conditions and angles of attack was about  $70\%$  above the sting-mounted model. Beyond about  $40^\circ$ , no steady base pressure value could be reached with the sting-mounted model in either of the tested Mach numbers because of the severe effects of sting interference.

### TEST APPARATUS, EXPERIMENTAL TECHNIQUES, TEST CONDITIONS

#### WIND-TUNNEL FACILITY

All experiments were conducted in the NAVSHIPRANDCEN hypersonic tunnel, a facility equipped with a series of axisymmetric contoured nozzles with exit velocities ranging from  $M = 5$  to  $M = 10.0$  and an open-jet test section. The outside diameter of the jet is approximately  $13.5$  in. with a uniform (flow uniformity  $\pm 1.75\%$ ) core of approximately  $6$  in. The unit Reynolds number can be varied from  $8 \times 10^4$  to  $10^8/\text{ft}$  by varying the supply pressure over the range from  $15$  to  $600$  psia and varying the supply air temperature from ambient to  $2500^\circ\text{F}$ . A more detailed description is available in Reference 24.

#### MODEL DESCRIPTION

The  $10^\circ$  half-angle cone models were designed to be injected into the flow field and released to fall freely through the hypersonic test section. They were  $6$  in. long with a nose radius of  $0.003$  in. and a base diameter of approximately  $2$  in. The skin was machined from corrosion-resistant steel that was polished and chrome plated to provide abrasion resistance. These models were capable of measuring base pressure distribution at various roll angles, angles of attack, and Reynolds and Mach numbers. Figure 1 shows an exploded view of the cone model, and Fig. 2 is the schematic drawing of the interior.

A conical brass weight was attached to the forward interior to provide for gross center of gravity adjustment. Threaded slugs within the weight were used for fine trim. Four differential pressure transducer telemeters were housed in a split, filled Teflon insert; the power supply leads were brought forward and connected in parallel to three mercury cells. The battery pack was clamped on the front half of the insert. The transducer measuring ports were connected through thick-walled flexible plastic tubing to brass nipples on the base orifice plate. A soft rubber plug was mounted in the Micarta base

plate, and in conjunction with a vacuum pump and hypodermic needle, served as a self-sealing valve for evacuation of the model interior (transducer reference pressure volume). A threaded bezel provided clamping force for the O-ring seal located between the orifice plate and model skin.

## INSTRUMENTATION AND DATA ACQUISITION SYSTEM

### Pressure Sensors

As previously mentioned, the free-flight model was equipped with four differential pressure transducer telemetry packages. These units were based on a Harrison design<sup>25</sup> and were fabricated by JPL. The telemeters utilized ultrastable Colpitts oscillators which were operated at center frequencies between 106 and 137 MHz. The oscillators were frequency modulated by the variable capacitance-type pressure transducers. The telemetry assembly consisted of four major components: a printed circuit inductor, a variable capacitance-type differential pressure transducer, a battery package, and a microminiature package of pellet-type construction for all other circuit components. The transducer sensing element was a 0.00025-in.-thick prestressed metal diaphragm soldered over the reference port case and separated electrically from the pressure port. The stress level of the diaphragm determined the sensitivity of the unit. The diaphragm and the inner surface of the pressure port formed the variable parallel plate capacitor. The various components of the unit were rigidly encapsulated in epoxy potting to provide thermal isolation and shock resistance.

The rise time of the pressure telemeters was about 0.5 msec without tubing, and their thermal stability was good. Harrison found that a temperature increase of 100°F at atmospheric pressure produced a 2.7% increase in the oscillator frequency and a 0.1% change in the full-scale sensitivity calibration. The temperature response time was about 3 min. There was little or no change in the telemeter performance over a temperature range from 30 to 200°F. Details on the construction of these units and their performance characteristics are given in the Harrison report.<sup>25</sup>

### Antenna Geometry

The signals from the telemetry units were intercepted by a complex antenna system that surrounded but was completely outside the hypersonic jet flow. Since the system operated in near field in the confines of a steel housing, which contained the open jet, the optimum antenna geometry had to be

arrived at by trial and error. After an extensive pretrial period during which several antenna geometries were tested, satisfactory performance was achieved by using two electrically parallel folded dipoles with the elements arranged approximately in the shape of a parallelepiped.

By using this antenna geometry, signal strength versus roll angle studies were made for three (x,z) coordinate points within the expected flight envelope at  $\alpha = 0^\circ$ ,  $-30^\circ$ , and  $-60^\circ$ . In general, signal strength values decreased below an acceptable level only over isolated areas amounting to 5 to 10% of roll angle each. It was further found that the transducer center frequency was independent of pitch and roll angles. Figure 3 depicts the final version of the antenna system, the drop mechanism, and the model installed in the hypersonic tunnel.

### Drop Mechanism

Prior to its injection into the hypersonic jet stream, the model was guided by a specially constructed drop mechanism that held it at a predetermined pitch angle and guided it down into the stream. As the model was completely submerged into the inviscid core of the flow, the restraining arms opened and released the model smoothly without imparting any side force or yawing moment. The vertical speed of the model was determined by the release height of the carriage. Four tension springs ensured that the restraining arms moved out of the flow field within 10 msec after model release so that they did not disturb the flow around it. The drop sequence had been so automatized that once the circuitry was energized, a multicam timer took over. The drop mechanism was calibrated to determine the correct location of the trigger switch so that the model was released at 0.25 ( $\pm 0.1$ ) in. above the point where the carriage was mechanically restrained. This ensured that the model was released smoothly and very nearly at the same position in the stream. Calibration data showed that spring-mass system of the restraining arms and attached coil springs had a natural frequency of about 20 msec/cycle and the motion was damped out within 3 cycles.

After model release into the stream, the carriage impacted on a rubber bumper which caused it to bounce upward about 3 in. The natural frequency of this motion was such that the carriage and the release arms were completely removed from the stream 10 msec after release and only 200 msec later (well after the model had left the stream) did it return again for the second cycle of its damped oscillation.

## 9th Navy Symposium on Aeroballistics

A series of drops at varying carriage heights (between 0 and 20 in. above the flow centerline), corresponding to a range of terminal release velocities, provided data for the determination of (a) terminal release velocities as a function of drop height and (b) trigger switch location as a function of drop height; see Fig. 4.

### Signal Processing and Data Acquisition Systems

As mentioned earlier, the signals from the telemetry oscillator were beamed to a complex antenna system. This antenna system was matched to a coaxial cable by using a Blonder-Tongue Model MT-283 matching transformer and a signal splitter. Two preamplifiers (Jerrold Model 2440) were then used in cascade to obtain at least a 40 dB gain for driving the signal tapoffs (Jerrold Model UT-22W). Four tapoffs were used to couple the input signals to the four FM receivers. The resulting isolation was at least 31 dB and feed-through losses were less than 0.25 dB for the frequency range from 100 to 140 MHz.

The RF and oscillator stages of the tuners (McIntosh Model Type MR71) were modified to provide reception in the band from 100 to 140 MHz. An a-c voltage regulator (Sorensen Model AC1000) was used to maintain tuner line voltages within  $\pm 0.1\%$ . Tuner outputs were then fed into four amplifier amplifiers (Beckman Model C-44) which in turn drove the 600-Hz Type 7-323 galvanometers in a recording oscillograph (C.E.C. Type 5-124). Figure 5 is a block diagram of the signal processing network.

Ten channels recorded the incoming data on the oscillograph. Four processed the pressure signals, four measured the signal strength of each transducer channel network, one recorded the solenoid trigger release signal, and one recorded the output signal of a 1000-Hz reference timer. Figure 6 shows a sample of the oscillograph record.

The motion of the model was recorded by two high-speed motion picture cameras: (1) a Photsonics camera recorded the yawing and rolling motions of the models at the rate of 1000 frames/sec and (2) a Hycam model (installed at right angle to the viewing window of the wind tunnel) recorded the pitching motions of the cone at about 2000 frames/sec. The output of the 1000-Hz reference timer, recorded on the oscillograph, was also recorded on film so that the film and oscillograph data could be synchronized. Both the film and oscillograph data were manually

digitized and reduced to useful form by data reduction procedures detailed later.

During the drop, the tunnel cab pressure was continuously monitored by a Datametrix Type 1014 Electronic Manometer and a Type 511-3 Barocel capable of measuring pressures between 0 and 1 psi on seven consecutive scales ranging from 0.001 to 1.0 psi full scale. The instrument had been calibrated and certified to an accuracy of  $\pm 0.1\%$  on each scale by the Bureau of Standards. The accuracy was very important since this measurement provided the reference pressure values to which the base pressure signals were related in order to determine their absolute levels.

Since the data acquisition and processing system was rather complex and had to be synchronized with the model carriage release and solenoid release signals, a timer mechanism took over all functions as soon as wind-tunnel free-stream conditions were established and a timer starter switch was manually activated; see Fig. 5.

### PRELIMINARY SYSTEM STUDIES

#### Pressure-Time Response

The available time for physical measurements is very limited for all free-flight model experiments; it is on the order of 10 to 50 msec and seldom exceeds 0.1 sec. Trajectory predictions showed an available flight time of about 65 msec in the hypersonic stream. As a final check on the instrument design, pressure response data were obtained in the expected pressure range for short connecting-tube transducer systems and correlated with some analytical formulas<sup>26</sup>. Figure 7 shows the key results for the design configuration. Measurements indicated that the time response within the expected pressure range did not exceed 5 msec.

#### Transducer Interactions and Calibration

Pick and Dawson<sup>24</sup> systematically studied the effects of close proximity on the simultaneous operation of transducer telemetry units. They evaluated such parameters as interaction as a function of transducer-to-transducer distances, center frequency spread and its effect on the interaction, change of sensitivity in relation to center frequency, center frequency shifts as functions of transducer-to-transducer distances, and the effects of common power supply and shielding.

The results showed that the interaction increase was approximately proportional to

the inverse 0.65 power of the edge-to-edge distance and that the center frequency spread had the most significant effect on the interaction.

The frequent interaction calibration measurements showed that the interaction errors did not exceed  $\pm 1.3\%$  for pressures up to 3.0 mm Hg. In most cases, the interaction error was within  $\pm 0.5\%$ . The instrumented model was recalibrated daily with known pressure inputs. Corrections to compensate for interaction errors were contained in the calibration. The daily calibration results showed that all the transducers were linear within  $\pm 1.5\%$  and day-to-day repeatability was good.

#### TEST CONDITIONS

Thorough surveys of Mach number distribution and temperature distribution were undertaken for each test speed. The results showed that in the jet core (11 in. horizontal length, 6 in. vertical height, and 4 in. width) where the model trajectories were located, the Mach number values were defined as  $M = 5.30 \pm 0.11$ ,  $6.34 \pm 0.11$ , and  $9.94 \pm 0.11$ .

Measurements indicated that steady flow was established within 5 sec after startup. To ensure steady conditions and provide for time lag in the cab pressure sensor system, all model drops were initiated at least 15 sec after tunnel start.

The settling chamber temperature, upstream of the nozzle throat, was continuously monitored during runs by using a Chromel-Alumel thermocouple. Preliminary measurements established the temperature drop in the nozzle between the monitoring thermocouple and the test section for each stagnation condition. This information was used in computing the free-stream Reynolds number. The temperature differential between the settling chamber and test section ranged between 30 and 80°F depending on time and stagnation pressure.

Variations in actual unit Reynolds numbers from run to run due to particular tunnel conditions were within  $\pm 8\%$  of the average values in all tested cases (the average unit Reynolds number values were 6.2, 6.4, 6.9, 3.0, 11.2, 11.4,  $10.7 \times 10^6/\text{ft}$ ) and contributed little to the overall inaccuracies of the data.

In all, the total error in the measured base pressure data due to instrumentation, interaction, and time response errors was

estimated to be within  $\pm 5\%$ .

#### TEST PROGRAM

Table 1 outlines the test program and the main parameters investigated. For each model drop, four data points were obtained at three different radii of the base area and at centerline. For a given flow condition and angle of attack, a series of 12 drops at 30° roll-angle increments provided good definition of the complete base pressure distribution. More than 450 data drops were conducted at seven separate flow conditions, and more than 90% of them were satisfactory.

TABLE 1

Test Program

M	Re/ft $\cdot 10^6$	$\alpha^\circ$
6.34 $\pm 0.11$	6.2 $\pm 0.5$	0 - 60
6.34 $\pm 0.11$	11.2 $\pm 0.7$	0 - 54
6.34 $\pm 0.11$	3.0 $\pm 0.2$	0 - 80
9.94 $\pm 0.11$	6.4 $\pm 0.3$	0 - 80
9.94 $\pm 0.11$	11.4 $\pm 0.6$	0 - 70
5.20 $\pm 0.11$	5.9 $\pm 0.4$	0 - 50
5.30 $\pm 0.11$	10.7 $\pm 0.7$	0 - 45

#### DATA REDUCTION

Two digital computer programs were developed to reduce data in useful forms. The first converted film data to model pitch angle; trajectory and aerodynamic coefficient ( $C_L$  and  $C_D$ ) information as functions of time. The second converted information from the oscillograph records to base pressure ratios  $p_B/p_\infty$  again as functions of time.

#### Reduction of High-Speed Motion Picture Data

The model motion and trajectory information for each run, obtained by the Hycam camera, was converted to useful form. Three points on the cone were digitized by using the apex and two selected points on the windward and leeward generators. The horizontal and vertical locations of each of these points were defined relative to a fixed fiducial coordinate system built into the camera. This information was recorded on punched cards for every fifth or tenth frame (a time interval of about 2.5 to 5.0 msec). The digitized frame position was defined in a time coordinate



## 9th Navy Symposium on Aeroballistics

system using timing marks which were recorded on the edges of the film. In this way, the position of the model could be defined with respect to any event (such as the opening of the release arm) and thus the measured base pressure data could be correlated with the model trajectory at any instant.

The program converted the raw digitized frame image to full-scale coordinates and applied corrections for optical lens distortions. With the cone converted to actual size, the center of pressure location and angle of attack were then determined from the digitized point locations using the formula:

$$x_{cp} = \frac{2L}{3 \cos^2 \theta_c} \quad (1)$$

but in the present experiment

$$x_{cg} = x_{cp} \quad (2)$$

This procedure was repeated for each digitized frame in a particular drop and the information was stored in the memory bank of the computer for further use. To compensate for small human errors in the manual process of digitization, a second order smoothing function was applied at this point to the stored center of pressure and angle of attack data as functions of time. The available information was sufficient for the calculation of the model terminal velocity ( $V_t$ ) before release, and this was used as initial vertical trajectory velocity input for computation of the equations of motion.

Two-dimensional curvilinear equations of motion were utilized to describe the trajectory of the center of gravity. These equations are expressed in rectilinear component form as:

$$s_x = \frac{1}{2} a_x t^2 \quad (3)$$

and

$$s_y = \frac{1}{2} a_y t^2 + V_t t \quad (4)$$

The horizontal component of the acceleration in the present investigation is given as:

$$a_x = \frac{g}{W} (C_D q_\infty S_B) \quad (5)$$

and the vertical component of the acceleration is:

$$a_y = \frac{g}{W} (W - C_L q_\infty S_B) \quad (6)$$

Substituting Equations (5) and (6) into Equations (3) and (4) yields:

$$s_y = \frac{g}{2W} (C_B q_\infty S_B) t^2 \quad (7)$$

and

$$s_y = \frac{g}{2W} (W - C_L q_\infty S_B) t^2 + V_t t \quad (8)$$

According to the modified Newtonian theory, the normal and axial force coefficients of a cone at any angle of attack can be expressed as:

$$C_N = \cos^2 \theta_c \sin 2\alpha \left[ \frac{\beta_u + (\pi/2)}{\pi} + \frac{1}{3\pi} \cos \beta_u (\cot \alpha \tan \theta_c + 2 \tan \alpha \cot \theta_c) \right] \quad (9)$$

and

$$C_A = \left[ \frac{\beta_u + (\pi/2)}{\pi} \right] \left[ 2 \sin^2 \theta_c + \sin^2 \alpha (1 - 3 \sin^2 \theta_c) \right] + \frac{3}{4\pi} \cos \beta_u \sin 2\alpha \sin 2\theta_c \quad (10)$$

where

$$\beta_u = \sin^{-1} \left( \frac{\tan \theta_c}{\tan \alpha} \right) \quad (11)$$

when

$$\alpha > \theta_c$$

and

$$\beta_u = \pi/2 \quad (12)$$

when

$$\alpha \leq \theta_c$$

Finally, the total drag and lift coefficients in terms of normal and axial force coefficients are given as:

$$C_D = C_N \sin \alpha + C_A \cos \alpha \quad (13)$$

$$C_L = C_N \cos \alpha - C_A \sin \alpha \quad (14)$$

In the computer program, Equations (7) to (14) were combined in functional forms as:

$$s_x = f(K, B, \alpha) t^2 \quad (15)$$

and

$$s_y = h(K, B, \alpha) t^2 + V_t t \quad (16)$$

where

$$K = K(W, \theta_c) \quad (17)$$

and

$$B = b(M, p_\infty) \quad (18)$$

Equations (15) to (18) were then used to obtain theoretical trajectory information from the measured time and angle of attack data based on point-to-point predictor-corrector techniques. Total drag and lift coefficients were also obtained using the measured trajectory, terminal velocity, and time information based on the film data in conjunction with Equations (7) and (8).

The final output provided angle of attack and trajectory results as functions of time and information on how they compared with theory together with measured and theoretical aerodynamic coefficients as functions of time. Provisions were also made for plotting all the data in graphical form.

#### Base Pressure and Force Reduction Program

Four oscillograph traces were recorded for each drop, one for each transducer. A sample output is shown in Fig. 6. The measured cab reference pressure and the free-stream total pressure and Mach number values were noted for each run together with a starting time corresponding to the time when the restraining arms released the model, the time when restraining arms completely retracted and interference free data are obtained and finally, the length of the useful running time. By using the reference pressure as a zero line, the pressure readings were taken in counts (100 counts/in.) along the vertical axis together with the corresponding time readings along the horizontal axis, again in terms of counts.

The reading on the vertical direction measured the difference between the reference and base pressures in counts. This was converted into pounds per in. by the transducer calibration constants. The resulting pressure was then either added to or subtracted from the reference pressure to yield absolute pressure values. The free-stream static pressure was determined from the Mach number and total pressure input data. The time readings were converted into milliseconds using the reference timing marks on the oscillograph. A maximum of eight pressure-time readings could be taken along any one trace.

The program output contained the run

number, Mach number and reference pressure, and all the inputs in counts. The base pressure ratios were tabulated in 5-msec intervals, starting from the initial time to the end of the run. A linear interpolation routine was used to obtain the intermediate values of  $p_B/p_\infty$ .

The total force on the model base is a function of the base pressure distribution. Generally, this is in the form:

$$F_B = \int_0^R \int_0^{2\pi} f(p_B) d\phi dr \quad (19)$$

To facilitate numerical computations, Equation (19) was approximated by:

$$\begin{aligned} F_B = & 0.0491 \left( \overline{p_{B_1}/p_\infty} * p_\infty \right) \\ & + 0.393 \left( \overline{p_{B_2}/p_\infty} * p_\infty \right) \\ & + 0.783 \left( \overline{p_{B_3}/p_\infty} * p_\infty \right) \\ & + 2.29 \left( \overline{p_{B_4}/p_\infty} * p_\infty \right) \end{aligned} \quad (20)$$

where  $\overline{p_{B_1}/p_\infty}$ , etc., were obtained by graphical integration of the plots of  $p_B/p_\infty$  versus roll angle ( $\phi$ ) (see Fig. 14 to 16) at the various nondimensional base radii.

The overall average base pressure then is computed from Equation (20) as:

$$\overline{p_B} = \frac{F_B}{S_B} \quad (21)$$

From this, the base pressure coefficient and base drag was obtained as:

$$C_{p_B} = \frac{\overline{p_B} - p_\infty}{q_\infty} \quad (22)$$

and

$$C_{D_B} = \frac{\overline{p_B} * \cos \alpha}{q_\infty} \quad (23)$$

At angle of attack, the base force also has a vertical component. This represents a lift force. In coefficient form this is expressed as:



$$C_{LB} = \frac{\overline{p_p} \star \sin \alpha}{q_\infty} \quad (24)$$

## DISCUSSION OF RESULTS

## BASE PRESSURE DISTRIBUTION

An important aspect of the experimental program was to measure the pressure distribution of the complete base area. This was necessary for the computation of the base pressure coefficients and base drag in all test conditions. Furthermore, these measurements provided an insight into the external flow field and recirculation region adjacent to the base. This in turn offers the possibility to formulate a new phenomenological model to serve as a more realistic basis for near wake computations.

Figure 8 to 10 show the variation of the base pressure, normalized by free-stream static pressure, as a function of angle of attack, Mach number and Reynolds number. Note that in each curve the base pressure at  $\alpha = 0^\circ$  is slightly higher than at  $\alpha = -10^\circ$  or  $-20^\circ$ . At or around  $\alpha = -10^\circ$ ,  $p_B/p_\infty$  was a minimum. There was relatively little variation in the centerline base pressure with angle of attack between  $\alpha = -10^\circ$  and  $-30^\circ$ . Schlesinger and Martellucci<sup>6</sup> found similar results for a  $10^\circ$  half-angle cone at  $M = 6.0$ , e.g., centerline base pressure values were lower at  $\alpha = -10^\circ$  than at  $0^\circ$ . However, beyond  $\alpha = -30^\circ$ , the base pressure ratio increases quite rapidly with angle of attack. A direct relationship was found between  $p_B/p_\infty$  and Mach number; for the same  $\alpha$  and Reynolds number, the base pressure ratio was lower for lower Mach number. This is in agreement with the results given by References 11, 28, and 29.

Further examination of the results in Figures 8 and 9 show that for  $M = 9.94$  and identical angle of attack conditions, increasing the Reynolds number caused a decrease in  $p_B/p_\infty$  values at identical  $\alpha$  conditions. The effect of Reynolds number seemed negligible for  $M = 5.30$ . These results provide some indications as to the state of the cone boundary layer as well as the flow conditions immediately downstream of the base. In addition to these results, temperature measurements and various flow visualization studies performed previously in a preliminary program indicated that the cone boundary layer and the base flow at  $M = 9.94$  were laminar in the unit Reynolds number and angle of attack range tested. This was in good agreement with measurements

made elsewhere<sup>5,11</sup>. Both the preliminary and present results indicate that conditions at the base at  $M = 6.34$  and  $5.30$  ranged from laminar at  $\alpha = 0^\circ$ , to transitional at moderate angles of attack, to turbulent at high angles of attack.

According to the measurements of Pate<sup>30</sup>, transition at  $\alpha = 0^\circ$  occurs at Reynolds numbers based on local inviscid conditions of about  $4 \times 10^6$ . At angles of attack, the transition Reynolds number decreases rapidly principally because of cross-flow formation in the boundary layer from the windward to the leeward side and vortex shedding action on the leeside. Both of these phenomena are connected with angle of attack; they first appear at  $\alpha \approx 0.8 \theta_c$  (where  $\theta_c$  is the semi-vortex angle of the cone), as was shown by Moore<sup>31</sup> and Tracy<sup>32</sup>, and increase in strength and effect as the angle of attack increases. The boundary layer cross flow and, more particularly, the leeward vortex shedding, causes instabilities in both the viscous and inviscid portion of the flow around the cone and in the near wake. Feldhuhn et al<sup>28</sup> measured the variation of transition Reynolds number with angle of attack and found that at  $M = 6.0$  and  $\alpha \geq 30^\circ$ ,  $Re_{\alpha}/Re_{\alpha=0} \approx 0.15$  where the quantity represents ratio of the transition Reynolds number at angle of attack relative to the transition Reynolds number at  $\alpha = 0^\circ$ . A preliminary investigation, with a  $9^\circ$  half-angle sting-mounted cone, undertaken prior to the main experiments showed that the recirculation region in the base at  $M = 6.3$  and  $Re = 1 \times 10^6/\text{ft}$  was transitioning when the angle of attack exceeded  $20^\circ$  and became turbulent at around  $30^\circ$ .

In the light of the aforesaid, it can be concluded that in the base region of the model and at  $M = 5.30$  and  $6.34$ , transition and possible turbulent flow conditions prevailed when  $Re = 6 \times 10^6/\text{ft}$  and the angle of attack exceeded  $20^\circ$ , whereas conditions were laminar at lower angles of attack. This is further substantiated on closer examination of Figures 11 and 12. These show the base pressure distribution along the vertical meridian for  $M = 6.34$  and  $5.30$  where the lowest point on the vertical scale corresponds to the windward generator and the highest point to the leeward generator. Reynolds number and angle of attack are independent variables in each graph.

At  $\alpha = 0^\circ$ , the base pressure distribution in the vertical meridian in all measured conditions showed a maximum value at the centerline and tapered off toward the edges. This is typical of the laminar conditions found in several investigations<sup>11,32,33</sup>.

As the angle of attack increased from  $\alpha = 0$  to  $-20^\circ$ , the general level of base pressure along the base region decreased relative to the zero angle of attack and the centerline pressure more particularly decreased even further than the edge values so that from the stagnation line to the centerline, base pressure distribution was nearly uniform (as was the case of  $Re = 3 \times 10^6/ft$ ,  $M = 6.34$  or  $M = 5.9$  at both Reynolds numbers) or decreased toward the centerline (see the two higher Reynolds numbers at  $M = 6.34$ ). In contrast, the base pressure ratio increased beyond the centerlines toward the leeward side in the meridian plane. This tendency was also noticeable at higher angles of attack. Cassanto<sup>33</sup> showed that the peak value of  $p_B/p_\infty$  shifted to the leeward side from the centerline and that the radial base pressure ratio also increased toward the leeward side when  $\alpha \geq 5^\circ$ . Although Cassanto's results were obtained at somewhat higher Mach numbers, it seems to apply qualitatively to the present data as well. The general uniformity of base pressure along the meridian plane as well as in the entire base region at  $-10$  to  $-30^\circ$  was usually within  $\pm 15\%$ ; this is considered to indicate transition or turbulent flow conditions. Martellucci and Ranlet<sup>9</sup> reported also that in the transition and turbulent flow regimes, the nonuniformity of the base pressure distribution decreased and ultimately diminished due to large mixing.

When the angle of attack increased further, the general level of the base pressure increased but the characteristic distribution stayed the same as indicated by decreasing base pressure from the most windward generator to a minimum point close to the centerline and thereafter an increase as the leeward side generator was approached. The level of base pressure was, in most cases, higher at the leeward side than at the windward side. Stetson and Friberg<sup>22</sup> explain this phenomenon by the fact that at large angles of attack, strong interactions occur between the base flow field and the leeward vortex flow field. They observed that the base pressure increased locally in regions adjacent to the minimum pressure region on the cone and attributed the effect to weak local shock wave systems. The pressures in the separated region on the leeward side were always larger than the base pressure, but the interaction between the two regions apparently caused a local increase around the neighborhood of the leeward meridian  $\pm 30^\circ$ . This is further confirmed by the analysis of the complete base pressure distributions at and beyond  $\alpha = -30^\circ$ , in particular when  $r/R = 0.71$  (see Fig. 14 and 15).

Schlieren photographs taken during the preliminary investigation showed that the incipient shock on the windward side of the cone became highly curved downstream of the model at high angles of attack. The shock appeared to turn toward the base centerline downstream of the recirculation region. It is conceivable that the incipient shock on the windward side deformed the inner shear layer causing a local expansion and consequent drop in local pressure. This drop of local pressure would be felt throughout the recirculation region and consequently, the base pressure close to the windward side within a  $\pm 20^\circ$  region would experience a drop toward the centerline. The combination of these effects would be a plausible explanation for the shape of the base pressure distribution at high angles of attack.

At  $M = 9.94$ , the cone boundary layer and base flow were laminar for the complete test range. Examination of Figure 13 reveals that at both  $Re = 6.4 \times 10^6/ft$  and  $Re = 1.1 \times 10^6/ft$  there was a maximum value for  $p_B/p_\infty$  at the centerline for  $0^\circ$  angle of attack. As the angle of attack increased to  $\alpha = -30^\circ$  and above, the general level of base pressure increased but in a very nonuniform way. From the edge to the centerline starting at the windward generator, the base pressures decreased or were nearly uniform toward the centerline. There they reached a minimum point and then increased rather abruptly toward the leeward generator where the base pressure level was 70 to 80% higher than at the centerline. This peculiar  $p_B/p_\infty$  distribution was apparently caused by the strong interaction between the base flow field and the leeward vortex flow field combined with the highly curved incipient shock wave that acted downstream of the base on the windward side and deformed the shear layer. Similar, but not identical, behavior was noted for the other two Mach numbers.

Figures 14 to 16 show examples of the base pressure distributions at three different radii ( $r/R = 0.24, 0.47$ , and  $0.71$ ) along the roll angle range of  $0$  to  $360^\circ$  for all three Mach numbers at  $Re = 6.0 \times 10^6/ft$ . These figures were partially analyzed in the preceding sections. However, there are some interesting points which have not been discussed yet. Notice in Figure 14 the minimum areas at roll angles of  $30$  and  $240^\circ$  in the vicinity of the base centerline ( $r/R = 0.24$ ) at  $\alpha = -40^\circ$ . Adjacent to these areas

local maximum points occurred at roll angles of 120 and 310°. This same phenomenon was repeated at angles of -10, -20, and -30°. At  $M = 9.94$  (Fig. 16), there were minimum zones at roughly 90° from the vertical meridian plane and maximum zones adjacent to the leeward meridian. The fact that local maxima and minima were close to the center area but occurred only at certain spots indicate local flow reattachments due to the interaction of rolled up vortex sheets from the leeward side and the recirculation region. Apparently this interaction resulted in an intensive local mixing and secondary reattachment. The phenomenon is nonasymmetric. At the lowest Mach number tested (see base pressure distribution in Fig. 15), this phenomenon was much less pronounced than for the higher Mach numbers. A possible explanation is that the pressure gradients within the base region were much smaller than in the other cases because intensive turbulent mixing alleviated the secondary reattachment.

## AERODYNAMIC COEFFICIENTS AT THE MODEL BASE

Base pressure coefficients, as defined by Equation (22) and evaluated by Equations (20) and (21), are shown in Fig. 17 and 18. Strong Mach number dependence was evident from the results. At  $\alpha = 0^\circ$ , the  $|C_{p_B}|$  value was about 50% larger at  $M = 5.30$  than at  $M = 6.34$  but 4 to 7 times as large as the base pressure coefficient at  $M = 9.94$ . The differences decreased as the angle of attack increased. Around  $\alpha = -10$  to  $-20^\circ$ ,  $C_{p_B}$  was minimum for all test conditions and thereafter increased with increasing angle of attack. The base pressure coefficients did not depend significantly on Reynolds number throughout the test envelope. The only exception was at  $M = 9.94$  and  $\alpha = -10^\circ$  where  $C_{p_B}$  at  $Re \approx 6 \times 10^5/\text{ft}$  was only 50% of the base pressure coefficient value measured at  $Re \approx 1 \times 10^6/\text{ft}$ . The Reynolds number effect is evident when one compares Fig. 17 and 18.

The base drag coefficients for  $Re \approx 6 \times 10^5$  and  $1 \times 10^6/\text{ft}$  are shown in Fig. 19 and 20, respectively. Mach and Reynolds number effects were quite insignificant throughout the test envelope. The base drag coefficient decreased between  $\alpha = 0$  and about  $\alpha = -15^\circ$  and increased with increasing angle of attack thereafter. The measurements of base drag at  $\alpha = 0^\circ$  were in good agreement with data presented by Ward and Choate<sup>10</sup>. They found that at  $M = 10$  and  $Re \approx 3$  to  $6 \times 10^5$ , the base drag was close to 0.008. The present measurements showed very similar results in  $C_{D_B}$  values at  $M = 9.94$  (see Fig. 19 and 20).

Examination of the base drag to total drag ratio (if comparison is made between Fig. 19, 20, and 23 to 25) showed that at  $\alpha = 0^\circ$ , the base drag was about 15 to 18% of the total drag at  $M = 5.30$  and 6.34 and was in the neighborhood of 6 to 7% at  $M = 9.94$ . Results of other investigators corroborate these measurements. At  $\alpha \approx -10^\circ$ , the base drag to total drag ratio dropped to about 4 to 5% for all three Mach numbers. At  $\alpha = -20^\circ$  and beyond,  $C_{D_B}/C_{D_T}$  gradually decreased from about 1.7 to 1.1%.

When the model flew at an angle of attack, a base lift force was generated in addition to the base drag since the total force at the base was no longer parallel with the free-stream direction. Fig. 21 and 22 show the base lift coefficients as functions of  $M$ ,  $Re$  and  $\alpha$ . Apparently,  $C_{L_B}$  is nearly independent of  $M$  and  $Re$  and chiefly dependent on the angle of attack. The ratio of  $C_{L_B}$  to the total lift was in the order of 1 to 2% (if one compares Fig. 21, 22, and 26 to 28).

## TOTAL DRAG AND LIFT COEFFICIENTS

Figures 23 to 25 show the variation of the total drag coefficients with angle of attack for all test conditions. In addition to the measured values, the inviscid drag coefficients were computed utilizing the modified Newtonian theory. Equations (9) to (14) were used for these computations and the results are also shown on the graphs. The close agreement between measurements and theory is readily apparent, although some experimental scatter shows up in Fig. 24. Results of the investigation conducted by Ward et al<sup>3</sup> showed that at relatively low Mach numbers (below about 7) the viscous drag was insignificant and the total drag was the sum of the inviscid drag and base drag. But the base drag was only about 1.5% of the total drag at high angles of attack for the present investigation, as was discussed in the previous section, so the good agreement between measured and calculated drag coefficients was not surprising. At  $M = 9.94$ , the viscous drag became significant at  $\alpha = 0^\circ$  and consequently, the measured total drag coefficients deviated somewhat from the computed ones. The measured values were between  $C_D = 0.1$  and 0.12. These values were in good agreement with the measurements of Welsh et al<sup>2</sup> and Ward et al<sup>3</sup>.

Figures 26 to 28 show the total lift coefficients as functions of  $M$ ,  $Re$ , and  $\alpha$  for all test conditions. Lift coefficients, based on the Newtonian inviscid theory, were also computed using Equations (9) to (14). The computational results are shown as solid

curves on the graphs for comparison. Again, the measured and computed values are in good agreement.

#### MODEL TRAJECTORY RESULTS

In the great majority of the model drops, the model departure in the yaw plane was negligible, and therefore, use of two-dimensional curvilinear equations of motion was justified. Consequently, Equations (15) to (18), programmed for computer calculations, provided good approximations for semi-theoretical trajectory predictions in conjunction with predictor and corrector techniques. Figures 29 to 31 show that the measured and computed model trajectories were in good agreement throughout the Mach number and angle of attack range covered by the test program. Note that at lower angles of attack ( $|\alpha| < 20^\circ$ ), the agreement is relatively poor at  $M = 5.30$  and  $6.34$ . The steepness of the trajectories may account for this disagreement where the small inaccuracies of the data reduction procedure become relatively more significant than at trajectories where the horizontal distance is longer (i.e., trajectories corresponding to higher angles of attack). As a final comment on the trajectory calculations, it is worthwhile to mention that even when the model angle of attack changed significantly from point to point, the computed trajectory based on local angle of attack was in close agreement with the measured path.

#### CONCLUSIONS

The results can be summarized as:

- (1) The centerline base pressure normalized by free-stream static pressure, was relatively constant at angles of attack between  $-10$  and  $-30^\circ$ . Above  $-30^\circ$ ,  $p_B/p_\infty$  increased with increasing angle of attack.
- (2) An increase in Mach number caused an increase of the base pressure ratio.
- (3) At  $M = 9.94$ , laminar conditions prevailed throughout the entire test envelope. However, at  $M = 6.34$  and  $5.30$ , there was transition and turbulent flow in the near wake at angles greater than  $-20^\circ$ .
- (4) Measurements indicated a highly complex base flow region. A tentative explanation was offered, but much more flow field data are required to define all aspects of the base flow at high angles of attack in the hypersonic flow regime.

(5) Base drag at  $\alpha = 0^\circ$  represented a considerable fraction of the total drag but decreased to around 1.5% above the angle of attack at  $-20^\circ$ .

(6) Close agreement was found between the measured and predicted values of total lift and drag coefficients and when the modified Newtonian theory was used.

(7) The computed and measured trajectories were in good agreement.

#### REFERENCES

1. Griffith, B.J. and L.G. Siler, "Comparisons of Free-Flight and Wind-Tunnel Data on Slender Cones," Arnold Engineering Development Center, AEDC-TDR-64-272 (Dec 1964).
2. Welsh, C.G., G.L. Winchenbach and A.N. Madagan, "Free-Flight Investigation of the Aerodynamic Characteristics of a 10-Deg Semiangle Cone at Mach Numbers from 6 to 16," Arnold Engineering Development Center, AEDC-TR-69-63 (Apr 1969).
3. Ward, L.K., A.E. Hodapp and R.H. Choate, "Description of a Model Launcher and Techniques used for Obtaining Model Free-Flight Measurements in the VKI Continuous Flow Wind Tunnels at Mach Number from 1.5 through 10," Arnold Engineering Development Center, AEDC-TR-66-112 (Aug 1966).
4. Carpenter, P.W. and W. Tabakoff, "Survey and Evaluation of Supersonic Base Flow Theories," University of Cincinnati, Cincinnati, Ohio, NASA CR-97129 (Oct 1968).
5. Todisco, A. and A. Pallone, "Measurements of Laminar and Turbulent Near Wakes," AVCO, Everett, Mass., AIAA Paper No. 67-30 (Jan 1967).
6. Schlesinger, A. and A. Martellucci, "Wind-Tunnel Investigations of the Turbulent Near Wake of a Cone at Angle of Attack," GASL, N.Y., Tech Rpt 581 (Mar 1966).
7. Schmidt, E.M. and R.J. Cresci, "Near Wake of a Slender Cone in Hypersonic Flow," Polytechnic Institute of Brooklyn, Brooklyn, N.Y., AGARD Conference on Fluid Physics of Hypersonic Wakes, Vol. 1 (May 1967).
8. Martellucci, A. and A. Schlesinger, "Measurements in the Near Wake of a Cone at Mach 12," GASL, N.Y., Tech Rpt AD803-892 (Mar 1966).

## 9th Navy Symposium on Aeroballistics

9. Martellucci, A. And J. Ranlet, "Experimental Study of Near Wakes," GASL, N.Y., Tech Progress Rpt (Oct 1966).
10. Ward, L.K. and R.H. Choate, "A Model Drop Technique for Free-Flight Measurements in Hypersonic Wind Tunnels Using Telemetry," AEDC-TR-66-77 (May 1966).
11. Cassanto, J.M., N.S. Rasmussen and J.D. Coats, "Correlation of Measured Free-Flight Base Pressure Data for  $M = 4$  to  $M = 19$  in Laminar and Turbulent Flow," AIAA Paper No. 68-699 (Jun 1968).
12. Potter, J.L. and J.D. Whitfield, "Preliminary Study of the Effect of Unit Reynolds Number on Transition Sensitive Data," AEDC-TN-57-37 (AD 135338) (Feb 1957).
13. Bogdonoff, S.M., "A Preliminary Study of Reynolds Number Effect on Base Pressure at  $M = 2.95$ ," Journal of Aeronautical Sciences, Vol. 19, No. 3 (Mar 1952).
14. Whitfield, J.D., "Critical Discussion of Experiments on Support Interference at Supersonic Speeds," Arnold Engineering Development Center, AEDC TN-58-30 (Aug 1958).
15. Love, E.S., "A Summary of Support Interference at Transonic and Supersonic Speeds," NACA RM L53K12 (Jan 1954).
16. Kavanau, L.L., "Results of Some Base Pressure Experiments at Intermediate Reynolds Numbers with  $M = 2.84$ ," University of California, Institute of Engineering Research, Rpt No. HE-150-117 (Oct 1953).
17. Kavanau, L.L., "Base Pressure Studies in Rarefield Supersonic Flows," University of California, Institute of Engineering Research, Rpt HE-150-125 (Nov 1954).
18. Reller, J.O. and F.M. Hamaker, "An Experimental Investigation of the Base Pressure Characteristics of Non-Lifting Bodies of Revolution at Mach Numbers from 2.73 to 4.98," NACA TN-3393 (Mar 1955).
19. Sivier, K.R. and S.M. Bogdonoff, "The Effect of Support Interference on the Base Pressures of a Body of Revolution at High Reynolds Numbers," Princeton University Rpt No. 332, AFOSR TN-55-301 (Oct 1955).
20. Sieling, W.R., "The Effect of Sting Diameter and Length on Base Pressure at  $M = 3.88$ ," The Aeronautical Quarterly, Vol. 19 (Nov 1968).
21. Peckham, D.H., "Exploratory Tests on Sting Interference at a Mach Number of 6.8," RAE Tech Note Aero 2721 (Oct 1960).
22. Stetson, K.F. and E.G. Friberg, "Communication Between Base and Leeward Region of a Cone at Angle of Attack in a Hypersonic Flow," W-P AFB, ARL 69-0015 (DDC AD 696 584) (Jul 1969).
23. Pick, G.S., "Sting Effects in Hypersonic Base Pressure Measurements," NSRDC Test Rpt AL-85 (Dec 1971).
24. Ziegler, N.G., "The David Taylor Model Basin Wind-Tunnel Facility," DTMB Aero Rpt 1027 (Jul 1963).
25. Harrison, R.G. Jr., "A Pressure Telemeter for Wind-Tunnel Free-Flight Pressure Measurement," Jet Propulsion Laboratory Tech Rpt No. 32-763 (Feb 1966).
26. Pick, G.S., "A Study on Short-Time, Low Pressure Response in a Transducer System," Wash., NSRDC Test Rpt AL-74 (DDC AD 711 191) (May 1970).
27. Pick, G.S. and S.E. Dawson, "Multi-Channel Pressure Telemetry System for Base Pressure Measurements on Small Models," Proceedings, IEEE 3rd International Congress on Instrumentation in Aerospace Facilities (May 1969).
28. Feldhuhn, R., A. Winkelmann and L. Pasiuk, "An Experimental Investigation of the Flow Field Around A Yawed Cone," AIAA Journal (Jun 1971).
29. Soffley and Graber, "An Experimental Study of the Pressure and Heat Transfer on the Base of Cones in Hypersonic Flow," AGARD Proceedings, No. 19 (May 1967).
30. Pate, S.R., "Measurements and Correlations of Transition Reynolds Numbers on Sharp Slender Cones at High Speeds," AEDC-TR-69-172 (Dec 1966).
31. Moore, F.K., "Laminar Boundary Layer on Cone in Supersonic Flow at Large Angle of Attack," NACA TN 2844 (Mar 1963).
32. Tracy, R.R., "Hypersonic Flow over Yawed Circular Cones," Hypersonic Project Memo 69, California Institute of Technology (May 1963).
33. Cassanto, J.M., "Free-Flight Base Pressure Results for a Sharp Cone at Angle of Attack," G.E. Aerodynamics Laboratory Data Memo 70-88 (Mar 1970).

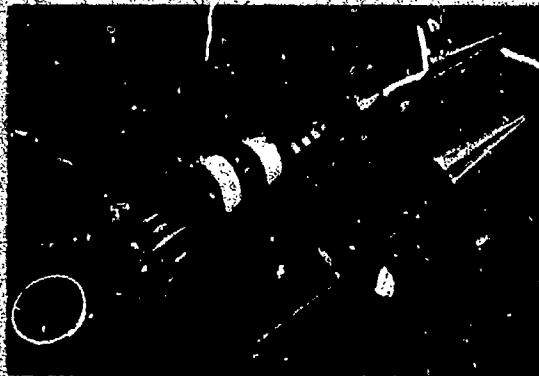


Figure 1 - Exploded View of Instrumented 10° Half-Angle Cone Base Pressure Model

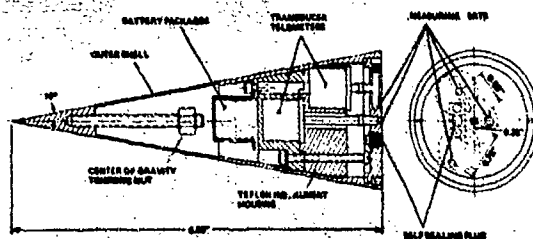


Figure 2 - Schematics of Model Interior

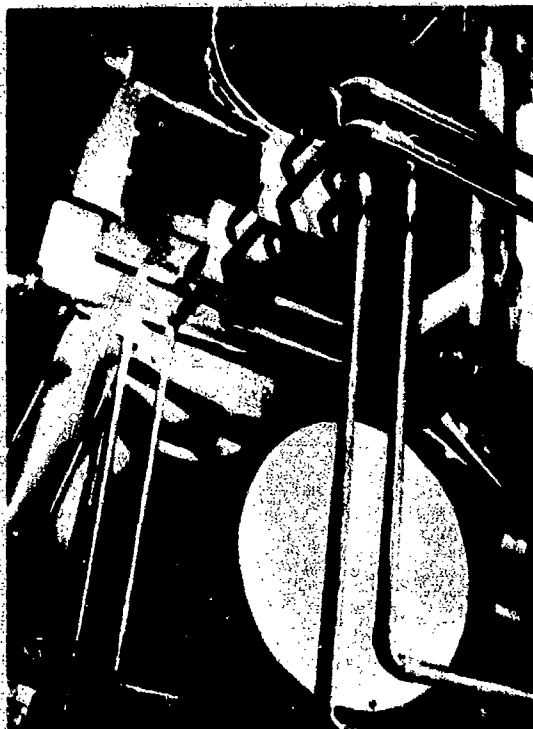


Figure 3 - Instrumented Cone Model and Antenna Installed in Hypersonic Tunnel

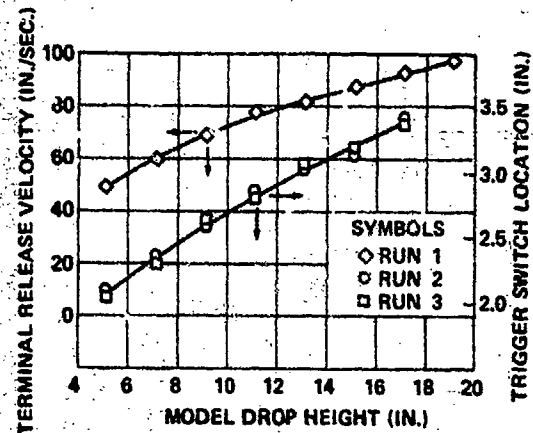


Figure 4 - Terminal Release Velocity and Trigger Switch Location as Functions of Model Drop Height

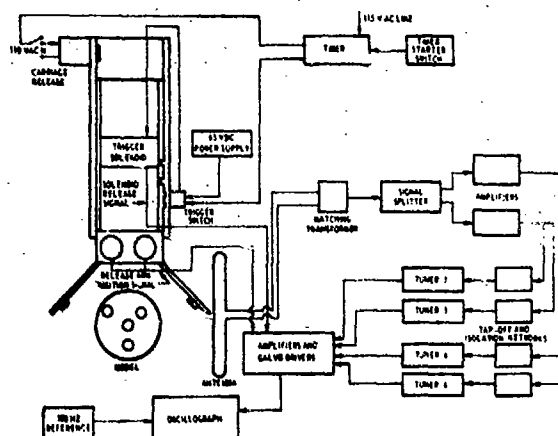


Figure 5 - Block Diagram of 10° Cone Model and Its Instrumentation in the Hypersonic Wind Tunnel

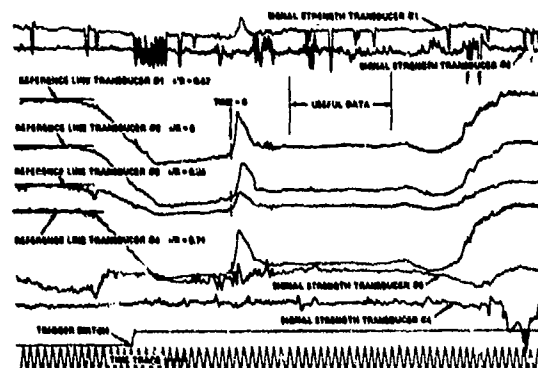


Figure 6 - Sample Oscillograph Record



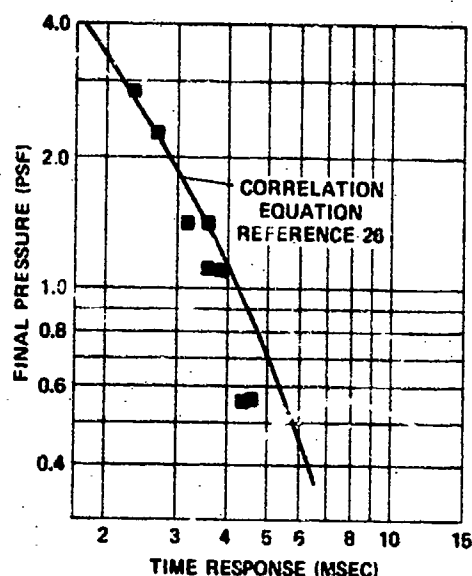


Figure 7 - Time Response Characteristics of the Transducer System

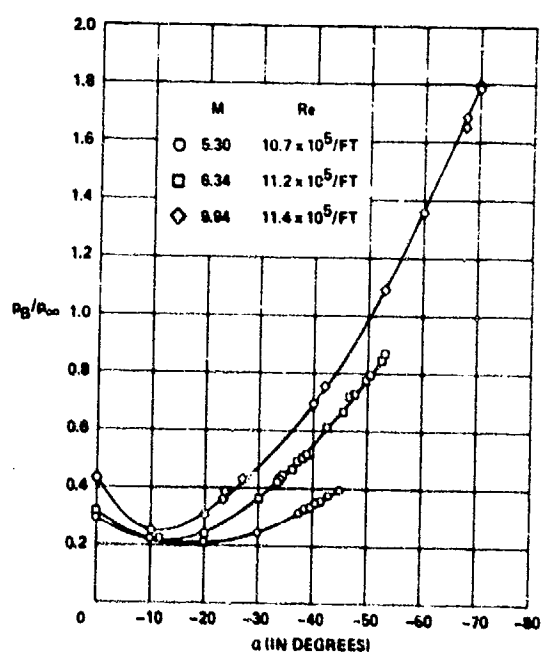


Figure 8 - Centerline Base Pressure Ratio as Function of Angle of Attack and Mach Number at  $Re = 1 \times 10^6/ft$

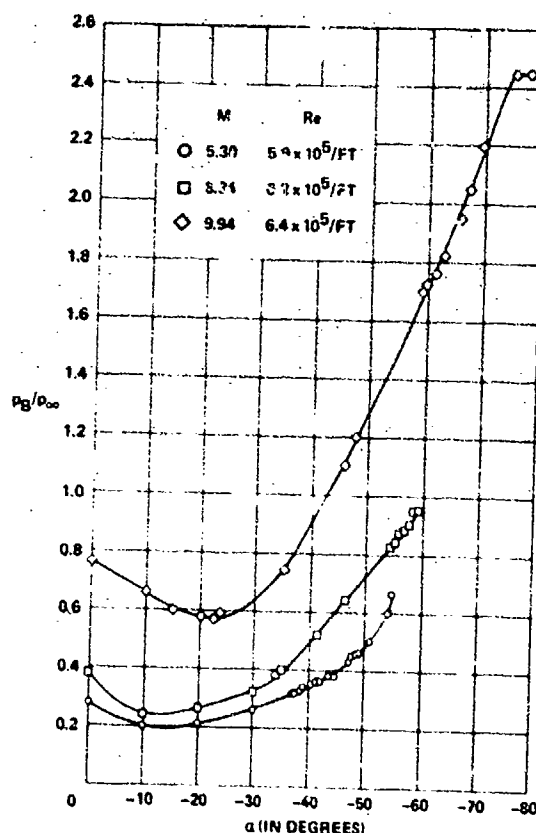


Figure 9 - Centerline Base Pressure Ratio as Function of Angle of Attack and Mach Number at  $Re = 6 \times 10^6/ft$

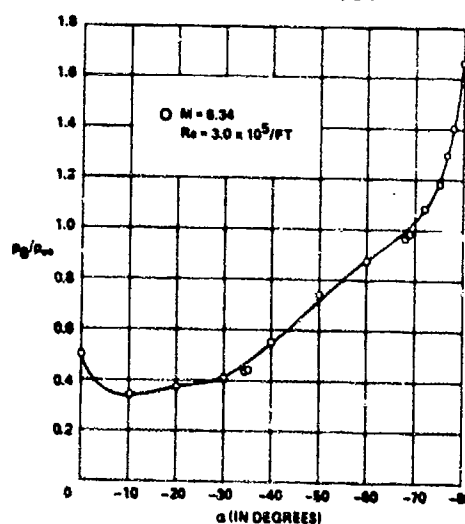


Figure 10 - Centerline Base Pressure Ratio as Function of Angle of Attack at  $M = 6.34$  and  $Re = 3 \times 10^6/ft$

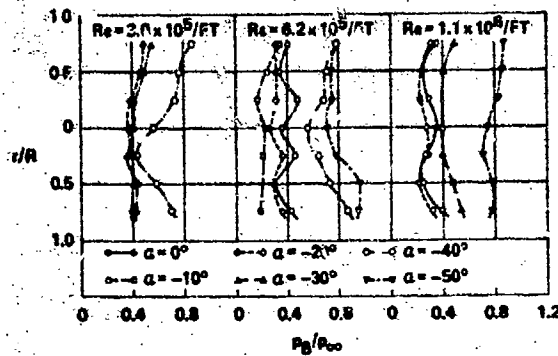


Figure 11 - Base Pressure Distribution in the Vertical Meridian Plane at  $M = 6.34$

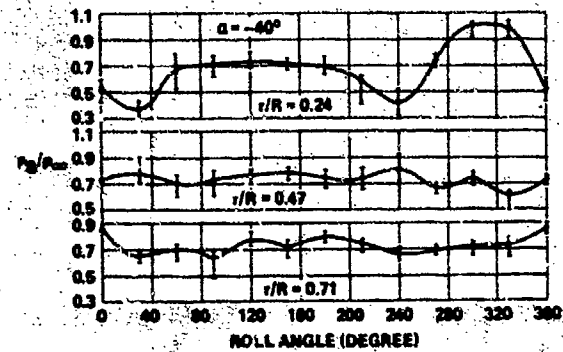


Figure 14 - Base Pressure Distribution at  $M = 6.34$  and  $Re = 6.2 \times 10^5/ft$

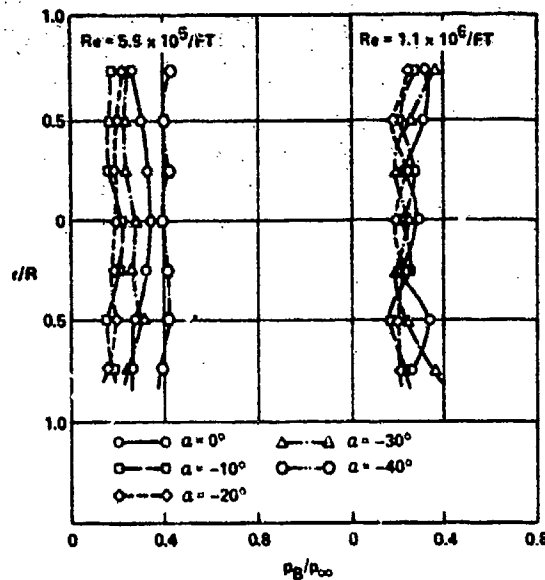


Figure 12 - Base Pressure Distribution in the Vertical Meridian Plane at  $M = 5.30$

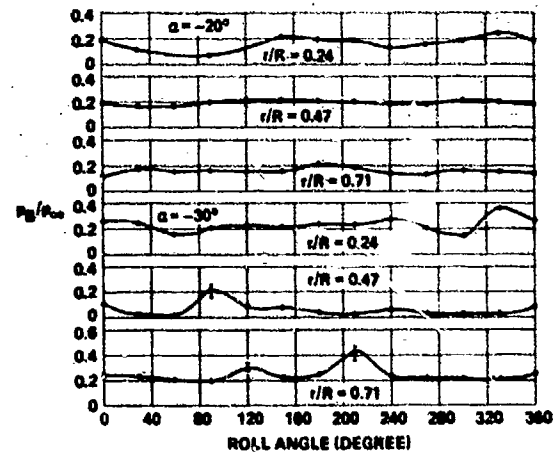


Figure 15 - Base Pressure Distribution at  $M = 5.30$  and  $Re = 5.9 \times 10^5/ft$

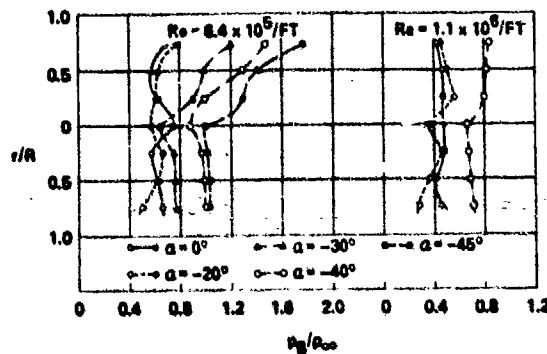


Figure 13 - Base Pressure Distribution in the Vertical Meridian Plane at  $M = 9.94$

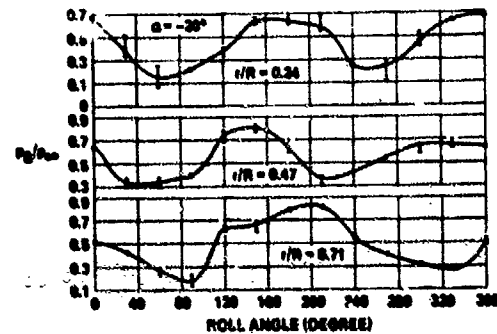


Figure 16 - Base Pressure Distribution at  $M = 9.94$  and  $Re = 6.4 \times 10^5/ft$



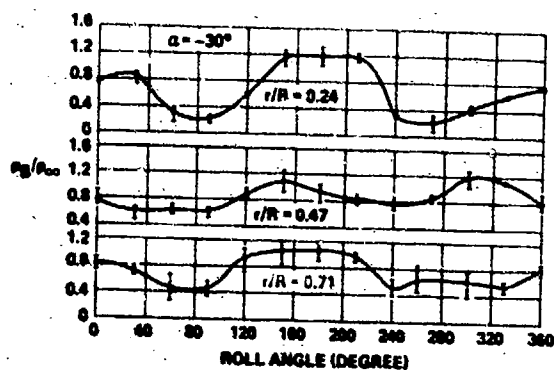


Figure 16 (Continued)

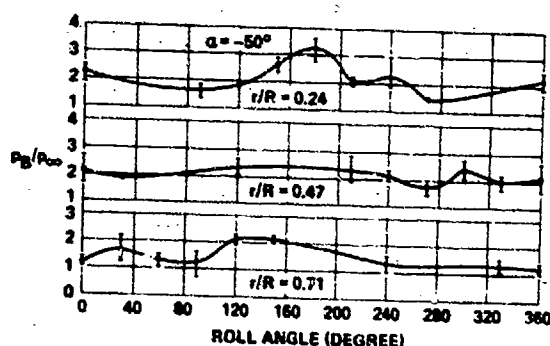


Figure 16 (Concluded)

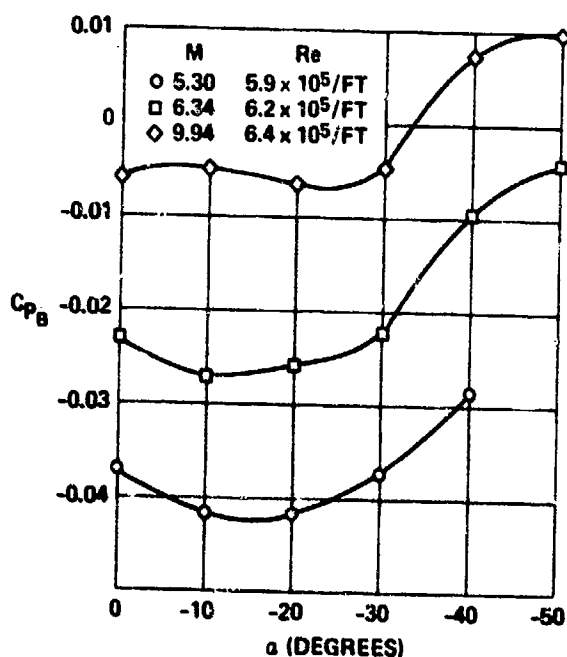


Figure 17 - Base Pressure Coefficients as Functions of Angle of Attack and Mach Number at  $Re \approx 6 \times 10^6/ft$

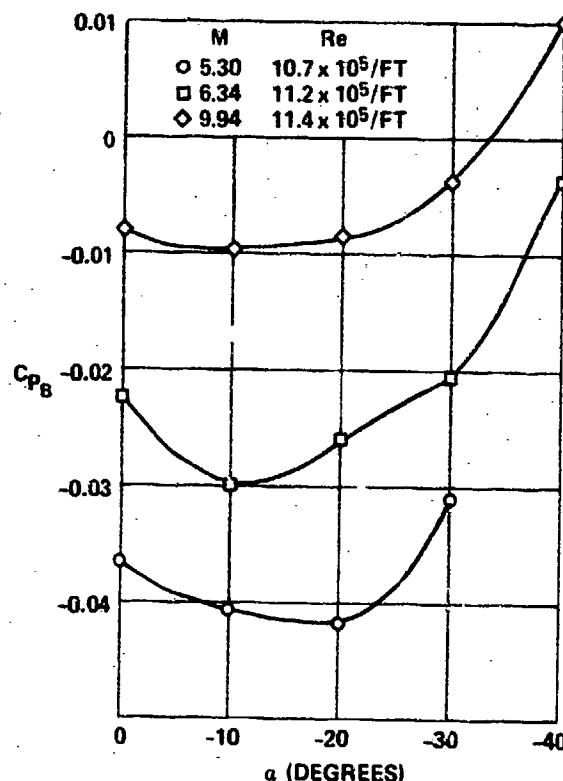


Figure 18 - Base Pressure Coefficients as Functions of Angle of Attack and Mach Number at  $Re \approx 1 \times 10^6/ft$

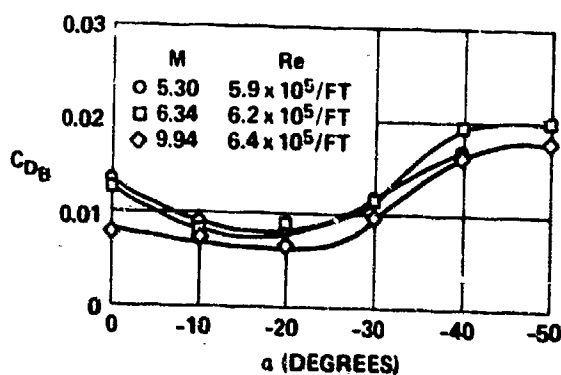


Figure 19 - Base Drag Coefficients as Functions of Angle of Attack and Mach Number at  $Re \approx 6 \times 10^6/ft$

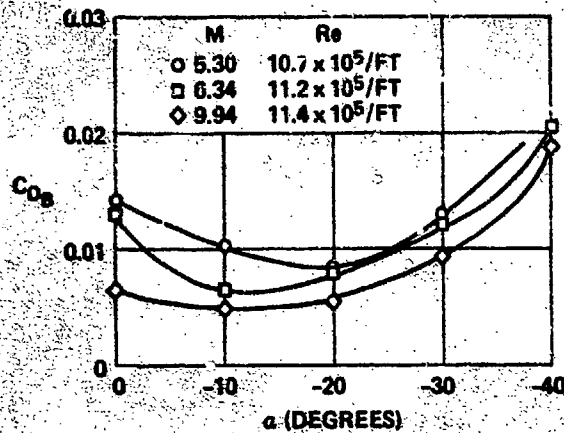


Figure 20 - Base Drag Coefficients as Functions of Angle of Attack and Mach Number at  $Re \approx 1 \times 10^6/\text{ft}$

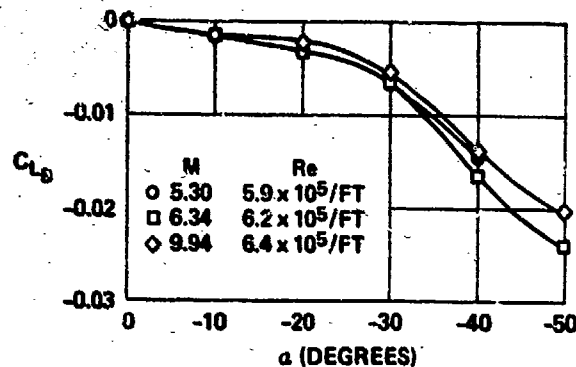


Figure 21 - Base Lift Coefficients as Functions of Angle of Attack and Mach Number at  $Re \approx 6 \times 10^5/\text{ft}$

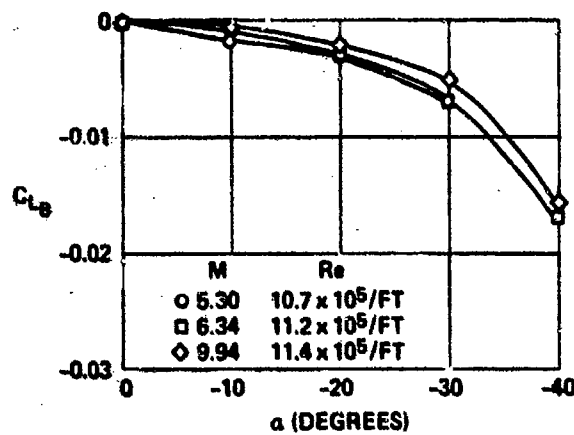


Figure 22 - Base Lift Coefficients as Functions of Angle of Attack and Mach Number at  $Re \approx 1 \times 10^6/\text{ft}$

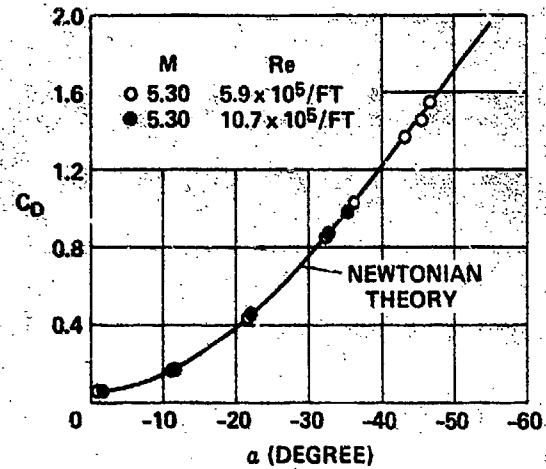


Figure 23 - Total Drag Coefficient as Function of Angle of Attack and Reynolds Number at  $M = 5.30$

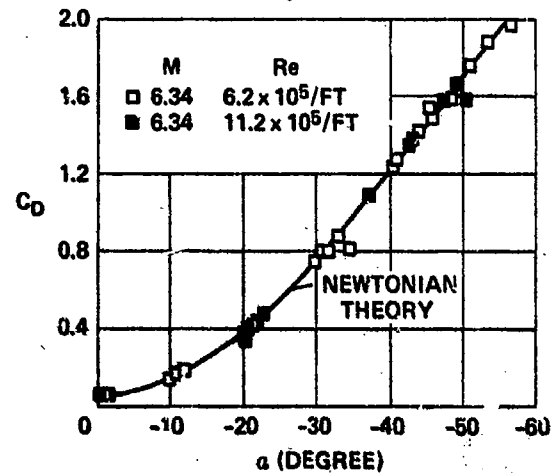


Figure 24 - Total Drag Coefficient as Function of Angle of Attack and Reynolds Number at  $M = 6.34$

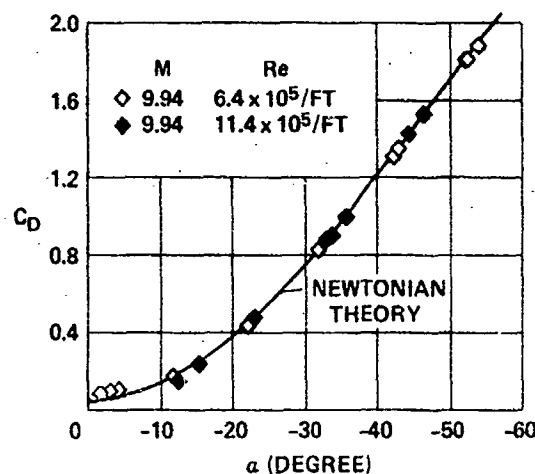


Figure 25 - Total Drag Coefficient as Function of Angle of Attack and Reynolds Number at  $M = 9.94$

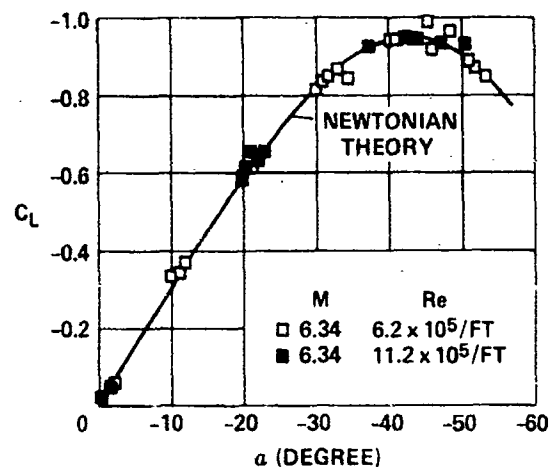


Figure 27 - Total Lift Coefficient as Function of Angle of Attack and Reynolds Number at  $M = 6.34$

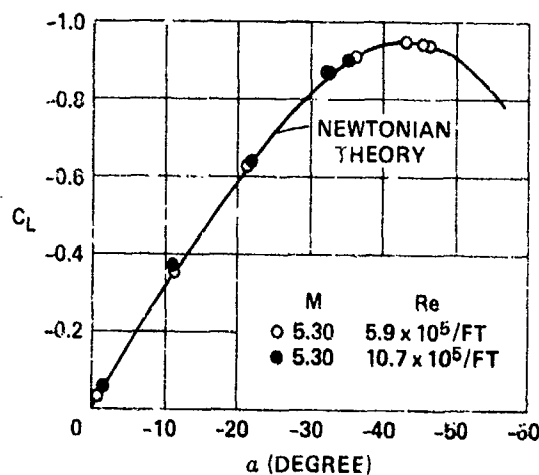


Figure 26 - Total Lift Coefficient as Function of Angle of Attack and Reynolds Number at  $M = 5.30$

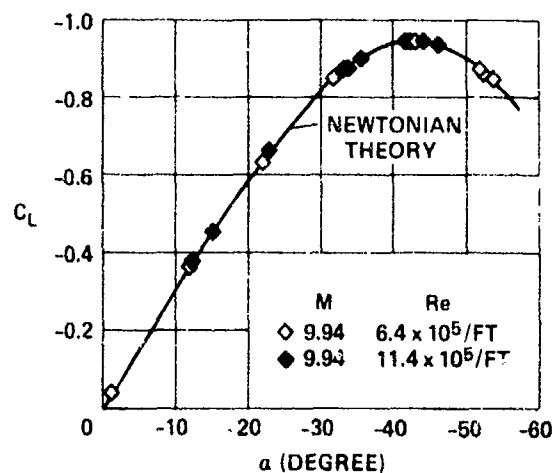


Figure 28 - Total Lift Coefficient as Function of Angle of Attack and Reynolds Number at  $M = 9.94$

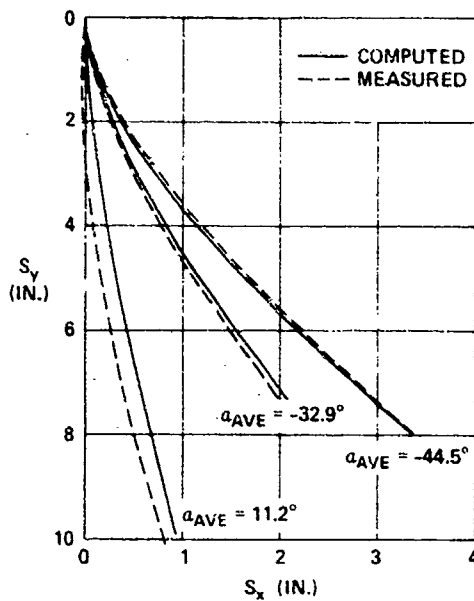


Figure 29 - Measured and Computed Model Trajectories at  $M = 5.30$  and  $Re = 5.9 \times 10^5/ft$

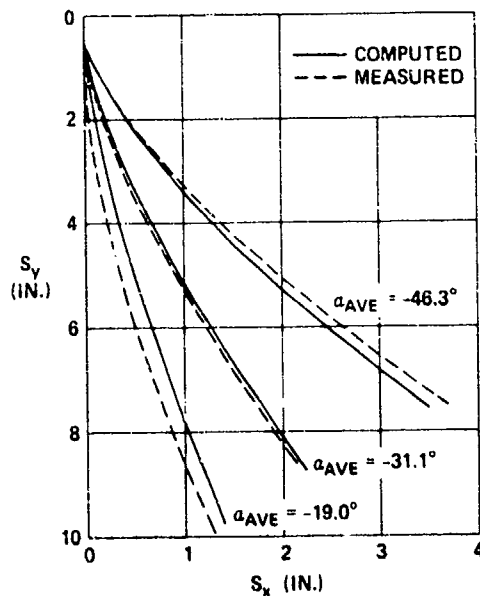


Figure 30 - Measured and Computed Model Trajectories at  $M = 6.34$  and  $Re = 6.2 \times 10^5/ft$

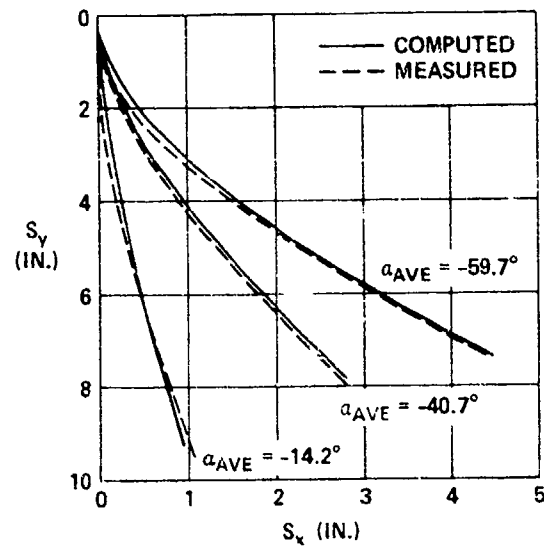


Figure 31 - Measured and Computed Model Trajectories at  $M = 9.94$  and  $Re = 11.4 \times 10^5/ft$

# INITIAL DISTRIBUTION

## Copies

1 ABRL/Lib  
 1 ABMDA/Lib  
 1 USAR&D/AMDA  
 1 Harry Diamond Labs/Lib  
 1 CHONR/ONR 100  
 1 NRL/Lib  
 2 ONR  
     1 ONR 430B/Cooper  
     1 ONR 521/Weinberg  
 1 USNA/Aero  
 1 NAVPGSCOL/Lib  
 1 NAVAIRDEVCEEN/813  
 1 NAVWPNCEN/Tech Lib  
 1 NSSNF Nav Stratetic Sys  
 2 NSWC  
     1 Library  
     1 KB/T. Clare  
 1 NAVMISCEN/Tech Lib  
 1 NAVSEA/Tech Lib  
 5 NAVAIRSYSCOM  
     1 AIR J38  
     1 AIR 03C  
     1 AIR 310  
     1 AIR 320  
     1 AIR 320C  
 12 DDC  
 1 Lib Maxwell AFB  
 1 USAFA/Lib  
 1 AFADTC/Tech Lib

## Copies

1 AEDC/Lib  
 1 AFWL Kirkland AFB/Lib  
 1 ARO  
 1 HOS NASA/Kurzweg  
 2 NASA Langley Res Cen  
     1 Library  
     1 D. Bushwell  
 1 NASA Lewis Res Cen/Lib  
 1 NASA Marshall SFC/Lib  
 1 Tech Inst Brooklyn/Spicer Lib  
 1 Tech Inst Brooklyn/Grad Lib  
 1 Case W Res U/E. Reshotko  
 1 Catholic U/P. Chang  
 1 U Calif Berkely/M. Holt  
 1 U Calif/Richmond FS  
     A. Oppenheim  
 1 U Calif Los Angeles/J. Cole  
 1 U Calif San Diego/P. Libby  
 5 Calif Tech/Pasadena  
     1 Aero Library  
     1 D. Coles  
     1 L. Lees  
     1 H. Liepmann  
     1 A. Roshko  
 1 U Cincinnati/A. Polak  
 1 U Colorado/Lib  
 2 Cornell U  
     1 Library  
     1 W. Sears

## Copies

1 U Delaware/J. Danberg  
 1 Georgia Tech/A. Duceffe  
 1 Harvard U/McKay Lib  
 1 Illinois Tech/M. Morkovin  
 1 Iowa State U/Lib  
 1 JHU Baltimore/S. Corrsin  
 3 JHU Appl Phys Lab  
     1 Library  
     1 F. Hill  
     1 L. Cronvich  
 1 U Maryland/J. Anderson/Aero  
 3 MIT  
     1 Aero Library  
     1 R. Probestein  
     1 A. Shapiro/ME Dept  
 1 U Michigan/Engr Lib  
 1 Michigan State U/Lib  
 2 New York U  
     1 Engr & Science Library  
     1 V. Zakkay  
 1 U North Carolina/Lib  
 1 NC State College/Raleigh  
     R. Truitt/Mech and Aero  
 1 NW 'J Tech Inst/Lib  
 2 Ohio State  
     1 Engr Library  
     1 Prof J. D. Lee/Aero-Astro  
 1 Notre Dame U/Engr Lib  
 1 Oklahoma State U/Engr Lib  
 1 Penn State U/Aero Lib  
 2 Princeton U  
     1 Prof S. Boydonoff/GD Lab  
     1 I. E. Vas/GD Lab

## Copies

2 Purdue U  
     1 Library/Engr  
     1 P. S. Lykoudis/Aero  
 1 Rensselaer Tech Inst/Lib  
 1 Rutgers/R. H. Page  
 1 Stanford U/Lib  
 1 Stevens Tech/M Engr Lib  
 1 U S Calif/J. Laufer  
 1 U Tenn SP Inst/J. T. Wu  
 1 U Texas Austin/AR Lab  
 1 U Toledo/Aero Eng Lib  
 1 U Va/Engr Lib  
     U Wash/Engr Lib  
 1 W Va U/Lib  
 2 AIAA  
     1 J. Newbauer  
     1 P. Marshall/Tech Info  
 1 Appl Mech Review SW Res Inst  
 1 Aerophysics Co/G. Boehler  
 1 Aero Res Assc/C. Donaldson  
 1 AVCO-Everett Res Lab/Lib  
 1 AVCO-MIS Sys Div/Lib  
 1 Boeing Co/E. Vogt  
 1 Chrysler Corp/Lib  
 1 Cornell Aero Lab/Lib  
 1 Fairchild Farmingdale  
     Engr Library  
 1 Gen Appl Sci Labs/Lib  
 1 GE Co/Daytona Beach

## Copies

1	GE Co/Philadelphia
1	GE Co/MSD Lib
1	GE Co/Re-Entry and Env Sys Div S. Scala
1	GE Co/R&D Lab H. Nagamatsu
1	Gen Dyn San Diego/Sweeney
1	Gen Dyn Convair San Diego Library
1	Gen Dyn Pomona/Lib
1	Gen Res Corp/Tech Info
1	Grumman A/C Eng Corp/Lib
1	Hercules Inc/AB Lab Lib
1	Hughes A/C Co CC/Tech Doc Ctr
1	Hughes A/C Co Fullerton/Lib
1	Inst Def Anal/Lib
1	Los Alamos Sci Lab/Rep LIB
1	LTV Aero Corp/MSD-T-Lib
1	LTV Aero Corp/Vought Lib
2	Lockheed-Calif Co 1 Dept 03-10 1 Gen Library
1	Lockheed Mis and Space Co/Tech Info
1	McDonnell-Douglas/Huntington Be A. M. O. Smith
1	McDonnell-Douglas-E/St Louis
1	Marquardt A/C Corp/Lib
1	Martin Marietta/Sci-Tech Lib
1	MIT Lincoln Lab/Lib A-082

## Copies

1	N A Rockwell Columbus/Lib
1	N A Rockwell L A/Lib
1	Northrop NORAIR/Tech Info
1	Philco-Ford Corp A. Demetriades/Aero
1	Rand Corp/Lib
1	Raytheon Co/Lib
1	Sandia Corp/Lib
1	Stanford Res Inst/Lib
1	TRW Houston/Lib
1	TRW Redondo Be/Tech Lib
1	United A/C Corp/Lib
1	Westinghouse/Astro Lab Lib

## CENTER DISTRIBUTION

Copies	Code	
1	0000	CAPT P. W. Nelson
10	1600	H. R. Chaplin
11	1660	
	1	J. H. Nichols
	10	G. S. Pick
30	5614	Reports Distribution
1	5641	Library (C)
1	5642	Library (A)
2	5643	Aviation Collection